The Astrophysical Journal, 962:36 (16pp), 2024 February 10 https://doi.org/10.3847/1538-4357/ad165e

The One-hundred-deg^2 DECam Imaging in Narrowbands (ODIN): Survey Design and Science Goals

Kyoung-Soo Lee[1], Eric Gawiser[2], Changbom Park[3], Yujin Yang[4], Francisco Valdes[5], Dustin Lang[6], Vandana Ramakrishnan[1], Byeongha Moon[4], Nicole Firestone[2], Stephen Appleby[7,8], Maria Celeste Artale[9], Moira Andrews[1], Franz Bauer[10,11,12], Barbara Benda[2], Adam Broussard[2], Yi-Kuan Chiang[13], Robin Ciardullo[14,15], Arjun Dey[5], Rameen Farooq[2], Caryl Gronwall[14,15], Lucia Guaita[9], Yun Huang[1], Ho Seong Hwang[16,17], Sang Hyeok Im[16], Woong-Seob Jeong[4], Shreya Karthikeyan[18], Hwihyun Kim[5], Seongjae Kim[4], Ankit Kumar[9], Gautam R. Nagaraj[14,15], Julie Nantais[9], Nelson Padilla[19], Jaehong Park[3], Alexandra Pope[20], Roxana Popescu[20], David Schlegel[21], Eunsuk Seo[22], Akriti Singh[9], Hyunmi Song[22], Paulina Troncoso[23], A. Katherina Vivas[24], Ann Zabludoff[25], and Alfredo Zenteno[24]

[1] Department of Physics and Astronomy, Purdue University, 525 Northwestern Avenue, West Lafayette, IN 47906, USA
[2] Physics and Astronomy Department, Rutgers, The State University, Piscataway, NJ 08854, USA
[3] Korea Institute for Advanced Study, 85 Hoegi-ro, Dongdaemun-gu, Seoul 02455, Republic of Korea
[4] Korea Astronomy and Space Science Institute, 776 Daedeokdae-ro, Yuseong-gu, Daejeon 34055, Republic of Korea
[5] NSF's National Optical-Infrared Astronomy Research Laboratory, 950 N. Cherry Avenue, Tucson, AZ 85719, USA
[6] Perimeter Institute for Theoretical Physics, 31 Caroline Street North, Waterloo, ON N2L 2Y5, Canada
[7] Asia Pacific Center for Theoretical Physics, Pohang, 37673, Republic of Korea
[8] Department of Physics, POSTECH, Pohang 37673, Republic of Korea
[9] Departamento de Ciencias Fisicas, Universidad Andres Bello, Fernandez Concha 700, Las Condes, Santiago, Chile
[10] Instituto de Astrofísica, Facultad de Física, Pontificia Universidad Católica de Chile, Campus San Joaquin, Av. Vicuna Mackenna 4860, Macul Santiago, 7820436, Chile
[11] Millennium Institute of Astrophysics, Nuncio Monseñor Sótero Sanz 100, Of 104, Providencia, Santiago, Chile
[12] Space Science Institute, 4750 Walnut Street, Suite 205, Boulder, CO 80301, USA
[13] Institute of Astronomy and Astrophysics, Academia Sinica, Astronomy-Mathematics Building, Roosevelt Road, Taipei 10617, Taiwan
[14] Department of Astronomy & Astrophysics, The Pennsylvania State University, University Park, PA 16802, USA
[15] Institute for Gravitation and the Cosmos, The Pennsylvania State University, University Park, PA 16802, USA
[16] Department of Physics and Astronomy, Seoul National University, 1 Gwanak-ro, Gwanak-gu, Seoul 08826, Republic of Korea
[17] SNU Astronomy Research Center, Seoul National University, 1 Gwanak-ro, Gwanak-gu, Seoul 08826, Republic of Korea
[18] Department of Astronomy, University of Maryland, College Park, MD 20742, USA
[19] Instituto de Astronomía Teórica y Experimental (IATE), CONICET-UNC, Laprida 854, X500BGR, Córdoba, Argentina
[20] Department of Astronomy, University of Massachusetts, Amherst, MA 01003, USA
[21] Physics Division, Lawrence Berkeley National Laboratory, 1 Cyclotron Road, Berkeley, CA 94720, USA
[22] Department of Astronomy and Space Science, Chungnam National University, 99 Daehak-ro, Yuseong-gu, Daejeon, 34134, Republic of Korea
[23] Escuela de Ingeniería, Universidad Central de Chile, Avenida Francisco de Aguirre 0405, 171-0614 La Serena, Coquimbo, Chile
[24] Cerro Tololo Inter-American Observatory/NSF's NOIRLab, Casilla 603, La Serena, Chile
[25] Steward Observatory, University of Arizona, 933 North Cherry Avenue, Tucson, AZ 85721, USA
Received 2023 September 18; revised 2023 December 14; accepted 2023 December 14; published 2024 February 5

Abstract

We describe the survey design and science goals for One-hundred-deg^2 DECam Imaging in Narrowbands (ODIN), a NOIRLab survey using the Dark Energy Camera (DECam) to obtain deep (AB $\sim$ 25.7) narrowband images over an unprecedented area of sky. The three custom-built narrowband filters, *N*419, *N*501, and *N*673, have central wavelengths of 419, 501, and 673 nm and respective FWHM of 7.5, 7.6, and 10.0 nm, corresponding to Lyα at $z = 2.4$, 3.1, and 4.5 and cosmic times of 2.8, 2.1, and 1.4 Gyr, respectively. When combined with even deeper, public broadband data from the Hyper Suprime-Cam, DECam, and in the future, the Legacy Survey of Space and Time, the ODIN narrowband images will enable the selection of over 100,000 Lyα-emitting (LAE) galaxies at these epochs. ODIN-selected LAEs will identify protoclusters as galaxy overdensities, and the deep narrowband images enable detection of highly extended Lyα blobs (LABs). Primary science goals include measuring the clustering strength and dark matter halo connection of LAEs, LABs, and protoclusters, and their respective relationship to filaments in the cosmic web. The three epochs allow for the redshift evolution of these properties to be determined during the period known as Cosmic Noon, where star formation was at its peak. The narrowband filter wavelengths are designed to enable interloper rejection and further scientific studies by revealing [O II] and [O III] at $z = 0.34$, Lyα and He II 1640 at $z = 3.1$, and Lyman continuum plus Lyα at $z = 4.5$. Ancillary science includes similar studies of the lower-redshift emission-line galaxy samples and investigations of nearby star-forming galaxies resolved into numerous [O III] and [S II] emitting regions.

Unified Astronomy Thesaurus concepts: Galaxy evolution (594); Lyα galaxies (978); High-redshift galaxies (734); Large-scale structure of the universe (902); High-redshift galaxy clusters (2007)

1. Introduction

In the hierarchical theory of structure formation, initial density fluctuations grow via gravitational instabilities and

form filaments, sheets, voids, before collapsing into virialized halos (Bond et al. 1996). These features, collectively referred to as large-scale structures (LSS), play an important role in determining a galaxy's fate by controlling the rate and the timescale of gas accretion and feedback, as well as the likelihood of galaxy–galaxy interaction.

Observational evidence supporting this expectation is abundant. At physical scales of ≈100's kpc, galaxies with a close companion tend to have enhanced star formation rates (SFRs) and follow a different mass–metallicity relation than that for isolated "field" galaxies (e.g., Ellison et al. 2008; Hwang et al. 2011). At cluster scales ($\lesssim$1 Mpc), the shape of the galaxy stellar mass function in cluster environment differs from that of average field (e.g., Baldry et al. 2006) in that fewer low-mass star-forming galaxies and a higher fraction of quenched galaxies are present. Similar trends persist in group-scale environments and in high-redshift ($z \approx 1$) clusters (Yang et al. 2009; Peng et al. 2010; van der Burg et al. 2020). Such environmental dependence may begin at $z \gtrsim 2$ (Lemaux et al. 2022), i.e., well before a large cosmic structure becomes fully virialized. At the largest scales (up to ≈10 Mpc comoving), the degree of galaxy clustering is a strong function of the stellar mass, SFR, luminosity, and spectral type (e.g., Giavalisco & Dickinson 2001; Norberg et al. 2002; Adelberger et al. 2005; Lee et al. 2006), suggesting that galaxies with larger stellar masses, higher SFR, and/or redder colors are hosted by more massive halos than their less massive, bluer counterparts.

At $z \gtrsim 2$, when the global star formation activity reached its peak (Madau & Dickinson 2014), the role of the LSS environment in galaxy formation remains under-explored. Many of the strong spectral features redshift to the infrared wavelength, making ground-based investigations difficult. Moreover, severe cosmological dimming requires long integrations on large-aperture telescopes to detect continuum emission and measure redshift even for relatively bright galaxies, rendering a complete spectroscopic survey unfeasible. While the James Webb Space Telescope and 30 m class telescopes will certainly alleviate these challenges, the small field of view probed by these facilities (typically, a few arcminutes on a side) is better suited for detailed follow-up studies of a few interesting systems rather than for general exploratory surveys large enough to probe the LSS.

At high redshift, Lyα emission provides one of the primary windows into the high-redshift universe (see review by Ouchi et al. 2020 and references therein), as it traces ionized and/or excited gas from star formation, black hole activity, and the gravitational collapse of dark matter halos. The Lyα emission strength from $z > 2$ galaxies is inversely correlated with stellar mass and internal extinction, meaning that Lyα emitters (LAEs) tend to have younger ages and lower SFRs than continuum-selected galaxies (e.g., Gawiser et al. 2006; Guaita et al. 2011). They are also less dusty than any other known galaxy population (Weiss et al. 2021). Given the relative ease of narrowband imaging compared to spectroscopy and the reduced projection effects of narrowband versus broadband selection, LAEs are the most efficient tracer of the underlying matter distribution at high redshift. The utility of LAEs for this purpose has been known for two decades (e.g., Hu & McMahon 1996; Ouchi et al. 2003; Gawiser et al. 2007; Kovač et al. 2007). Angular clustering measurements suggest that LAEs are hosted by moderate-mass halos (Gawiser et al. 2007; Guaita et al. 2010; Lee et al. 2014; Kusakabe et al. 2018). These traits give LAEs the lowest clustering bias among visible tracers of the underlying matter distribution. Finally, Lyα mapping via narrowband imaging offers an efficient alternative for collecting large galaxy samples in a well-defined volume with minimal contamination from foreground sources. The redshift precision, $\Delta z \sim 0.04$–0.06 is several times better than that afforded by the best photometric redshifts that can be derived using broadband filters ($\Delta z \sim 0.1$–0.2 at $z > 2$).

In this paper, we present the science goals and the design of the One-hundred-deg^2 DECam Imaging in Narrowbands (ODIN) survey, currently being carried out using the Dark Energy Camera (DECam; Flaugher et al. 2015) on the Blanco Telescope at the Cerro Tololo Inter-American Observatory. ODIN uses narrowband-selected LAEs as tracers of matter distribution at three different cosmic slices during Cosmic Noon to study the formation and evolution of galaxies and their association with dark matter halos.

This paper is organized as follows. In Section 2, we describe the key science goals of the ODIN survey and provide a broad context and an overview of each topic. Section 3 summarizes the survey parameters, detailing the filter transmission, and the key characteristics of the survey fields; additionally, we justify the imaging depths and present the expected outcomes upon completion of the survey. In Section 4, we discuss the general procedures guiding the data acquisition and reduction, and in Section 5, we describe the survey's existing and future data. Finally, in Section 6, we stress the legacy value of the ODIN data and the ODIN filters in advancing Galactic science. We adopt a ΛCDM concordance cosmology with $h = 0.7$, $\Omega_m = 0.27$, and $\Omega_\Lambda = 0.73$ and use comoving distance scales unless noted otherwise. All magnitudes are in the AB scale (Oke & Gunn 1983).

2. Primary ODIN Science Goals

The ODIN survey is designed to enable a multitude of science goals but is primarily geared toward understanding the formation and evolution of galaxies in the distant universe. ODIN probes the LSS in three narrow cosmic slices straddling the epoch of "Cosmic Noon" using custom-built narrowband filters. These filters sample redshifted Lyα at cosmic ages of 2.8, 2.1, and 1.4 Gyr ($z = 2.4$, 3.1, and 4.5), strategically placed to study the redshift evolution of galaxies and cosmic structures. When combined with the upcoming deep wide-field surveys to be conducted with the Rubin Observatory's Legacy Survey of Space and Time (LSST), the Nancy Grace Roman telescope, and Euclid, ODIN has the potential to reveal a wide range of astrophysical phenomena in the context of their LSS, as well as to measure the topology of LSS thereby constraining cosmological parameters. In what follows, we describe the primary goals of the ODIN survey.

2.1. Protoclusters, Cosmic Web, and Galaxy Inhabitants

Protoclusters are progenitors of the most massive gravitationally bound structures, i.e., clusters of galaxies. As such, identifying the sites of protoclusters allows us to find the member galaxies and directly witness their formation and evolution, thereby shedding light onto the physical processes that led to their early accelerated formation followed by strong and swift quenching that occurred at high redshift (e.g.,

Stanford et al. 1998; Blakeslee et al. 2003; Thomas et al. 2005; Eisenhardt et al. 2008; Mancone et al. 2010).

The limitations of studying protoclusters have been mutifold: first, clean and statistically robust samples of protoclusters have been difficult to obtain. The lack of readily identifiable signatures—such as a hot intracluster medium and/or a concentration of quiescent galaxies—in young, yet-to-be-virialized structures of mostly star-forming galaxies leads to a strong reliance on spectroscopy for finding protoclusters. Photometric redshifts from broad- and intermediateband filters can help with selection efficiency (e.g., Chiang et al. 2014), but few extragalactic fields have the data necessary to produce photo-z's with the requisite $\Delta z \approx 0.1$ precision (e.g., Shi et al. 2019; Huang et al. 2022).

Second, protoclusters subtend tens of arcminutes in the sky (Chiang et al. 2013; Muldrew et al. 2015) making member identifications challenging. Even if the general region of a protocluster were targeted, blind spectroscopy would be dominated by fore- and background interlopers. Finally, massive clusters are very rare. The most massive, Coma-like clusters ($M_{\rm today} \gtrsim 10^{15} M_{\odot}$) have a space density of $\approx$180 Gpc^{-3} (Reiprich & Böhringer 2002), corresponding to $\approx$2.3 deg^{-2} per unit redshift. Most surveys are ill-suited for discovering such sparsely distributed structures.

These difficulties explain why there are very few well-characterized protocluster systems (e.g., Dey et al. 2016; Cucciati et al. 2018). Despite the rapidly growing number of protoclusters and their candidates (e.g., Planck Collaboration et al. 2015; Toshikawa et al. 2018), there is a critical need for reliable markers or "signposts" of protoclusters. Though possible candidates are numerous (see Overzier 2016, and the references therein, but the candidates include radio galaxies, quasi-stellar objects, and Lyα nebulae), the extent of their success varies even when it can be measured. Moreover, the intersection of these markers, their respective selection biases, and their duty cycle (i.e., the typical timescale in which they stay visible) are currently unknown. Uniformly selected large samples of protoclusters are needed to address these questions.

ODIN uses LAE overdensities as tracers of massive cosmic structures. This is motivated by the fact that LAE samples suffer from much weaker projection effects than continuum-selected galaxies due to the narrow redshift interval and offer high sky density with contiguous coverage that cannot easily be achieved with spectroscopy. Additionally, studies of the few well-characterized protoclusters, such as SSA22, *Hyperion*, and PC217.9+32.3 (Steidel et al. 1999; Lee et al. 2014; Dey et al. 2016; Topping et al. 2018; Huang et al. 2022), suggest that LAEs trace the overall galaxy overdensity structures quite well, highlighting the systems' filament-like structures and knots.

In this context, one of the immediate goals of ODIN in advancing protocluster science are to procure a statistically complete sample of protoclusters via the identification of low-mass, low-luminosity galaxies, and to explore the intersectionality with structures of dusty star-forming galaxies (e.g., Planck Collaboration et al. 2015; Casey 2016), Lyman-break galaxies, extended Lyα nebulae, and radio galaxies. The survey volume and the target fields (Section 3) are chosen to allow for robust, statistically significant comparisons of the samples. A first analysis of how the ODIN-selected Lyα nebulae are located in the context of LAE-traced cosmic filaments and protoclusters is provided in Ramakrishnan et al. (2023). The ODIN fields coincide with the regions with the deepest Spitzer IRAC data (Section 5.2), which will enable a systematic search for the progenitors of giant cluster ellipticals, some of which are expected to have already been formed at high redshift (e.g., Thomas et al. 2005; Mei et al. 2006). Deeper IR data from Roman in the next decade will push the limit further. By combining statistical samples of protoclusters at three cosmic epochs, ODIN will be able to explore the formation histories of massive cluster ellipticals.

2.2. Extended Lyα Nebulae

Extended Lyα nebulae, also known as Lyα "blobs" (LABs), emit Lyα radiation with total line luminosities of 10^{43}–10^{44} erg s^{-1} on physical scales of 20–100 kpc (e.g., Francis et al. 1996; Steidel et al. 2000; Matsuda et al. 2004, 2011; Saito et al. 2006; Yang et al. 2009). This far exceeds the size of a single galaxy.

Given their extreme physical properties, the physical nature of LABs has astrophysical and cosmological implications. Some blobs are clearly produced by photoionization from intense radiation produced by embedded active galactic nuclei (AGNs), which themselves may or may not be visible at optical wavelengths (e.g., Kollmeier et al. 2010; Overzier et al. 2013; Yang et al. 2014). The recombination of ionized gas results in Lyα photons, which resonantly scatter and illuminate the surrounding H I gas. In a few spectacular cases around luminous QSOs (e.g., Borisova et al. 2016; Arrigoni Battaia et al. 2019) or multiple AGN, the scattered Lyα emission reveals cosmic filaments connected to the source (e.g., Cantalupo et al. 2014; Umehata et al. 2019). Alternatively, Lyα photons produced in the star-forming regions of embedded galaxies may scatter outward and power LABs (e.g., Laursen & Sommer-Larsen 2007; Cen & Zheng 2013; Chang et al. 2023). Shock heating of the gas in the circumgalactic medium by starburst-driven superwinds has also been proposed as a possible mechanism (e.g., Taniguchi & Shioya 2000).

Much attention has been given to LABs as potential signposts of gas accretion along cosmic filaments. As H I gas falls into the potential well of a dark matter halo and is heated to $\gtrsim 10^4$ K, a large fraction of the gravitational cooling radiation is expected to be emitted in Lyα (Haiman et al. 2000; Fardal et al. 2001). Although the tight correlation between stellar mass and SFRs, often referred to as the star-forming galaxy "main sequence" (e.g., Noeske et al. 2007), implies that the dominant mode of galaxy growth is through a relatively smooth and prolonged inflow of gas, direct and clear evidence for this inflow has been challenging to obtain.

Recent ultradeep integral field observations suggest that some LABs may indeed be powered by gravitational cooling. Daddi et al. (2021) showed that the morphology and kinematics of the extended Lyα emission around a galaxy group at $z = 2.91$ are consistent with gas inflow along multiple cosmic filaments converging onto the group. By studying extended Lyα emission around a handful of protoclusters or groups of galaxies, Daddi et al. (2022) reported tentative evidence that LAB luminosity correlates with dark matter halo mass (and thus with expected baryon accretion rate). These studies highlight the fact that direct detection of cold gas accretion near massive halos may be at the edge of the current observational reach.

Indeed, many known blobs are associated with galaxy overdensities (e.g., Shi et al. 2019) or lie near what appears to be a filament traced by galaxies (e.g., Erb et al. 2011).

Prescott et al. (2008) surveyed the region surrounding a very luminous, mid-IR-detected blob (Dey et al. 2005) and reported an overdensity of galaxies (also see Xue et al. 2017). A Lyα survey around a known protocluster at $z = 3.09$, SSA22, revealed multiple LABs (Steidel et al. 2000) residing in regions that appear to be converging filaments (Matsuda et al. 2004). Bădescu et al. (2017) noted that blobs tend to reside in the vicinity of protoclusters identified as LAE overdensities (also see Ramakrishnan et al. 2023). When combined with their high cosmic variance (Yang et al. 2010), the authors speculate that blobs may represent infalling proto-galaxy-groups.

To place definitive constraints on the physical origin(s) of LABs and their connection to cosmic structures, large and statistically complete samples of LABs are crucial. By detecting over 1000 bright LABs at three cosmic epochs, ODIN will produce the largest blob sample to date and enable robust measurements of the sizes, and luminosities, and redshift evolution of these objects. Auto- and cross-correlation function measures will inform us of typical masses of LAB host halos and their interrelation with known cosmic structures. When combined with the ODIN protocluster samples, it will be possible to determine whether or not LABs are reliable tracers of protoclusters, which in turn constrains the duty cycle of the LAB phenomenon.

2.3. Physical Properties of LAEs via LFs, Spectral Energy Distributions, and Clustering

LAEs represent a low-dust, high specific SFR stage of galaxy evolution, possibly consistent with galaxies undergoing initial starbursts (Partridge & Peebles 1967; Gawiser et al. 2007), making it important to fully characterize their properties. By detecting tens of thousands of LAEs situated in the wide and deep imaging fields in the equatorial and Southern sky, ODIN aims to greatly increase our knowledge of these galaxies' physical properties.

With the rapid increase in sophistication of cosmological hydrodynamic simulations and semi-analytic models of galaxy formation, it has become possible to test theoretical predictions for the distribution of directly observed galaxy properties including their continuum and emission-line luminosities and colors. LAEs offer a unique probe of the low-mass bulk of the high-redshift galaxy distribution, but connecting them with these models requires matching the observed distribution of Lyα emission strengths i.e., the Lyα luminosity function (LF), which report the number density of LAEs as a function of their Lyα luminosity (e.g., Gronwall et al. 2007; Ciardullo et al. 2012; Sobral et al. 2018); the large statistical samples enabled by ODIN's combination of depth and area and the strong interloper rejection enabled by deep photometry in multiple broadband filters will yield improved LF measurements at each redshift.

Deep rest-UV-through-near-IR broadband photometry of LAEs available in the ODIN fields (Table 2) will enable improved Spectral Energy Distribution (SED) fitting to measure SFR, stellar masses, and dust extinction. Vargas et al. (2014) found that, with broadband photometry significantly deeper than the narrowband photometry used to select LAEs, it was not necessary to stack LAE SEDs in order to obtain robust parameter fits. Sufficiently deep *u*-band-through-IRAC photometry is available in the CANDELS (Nayyeri et al. 2017; Merlin et al. 2021) and COSMOS2020 (Weaver et al. 2022) catalogs. Shallower *ugrizyK*+IRAC SEDs are available for stacked SED analysis of >30,000 LAEs in the 24 deg^2 field of Spitzer-HETDEX Exploratory Large Area (SHELA; Papovich et al. 2016; Wold et al. 2019; Stevans et al. 2021).

Clustering analysis allows us to connect LAEs to their host dark matter halos to answer key questions about galaxy evolution. Extended Press–Schechter theory (Sheth et al. 2001) and cosmological *N*-body simulations predict the clustering bias of dark matter halos as a function of the halo mass and redshift, and this has been used to learn that LAEs are hosted by dark matter halos with masses $\sim 10^{11}\,M_{\odot}$ (Gawiser et al. 2007; Guaita et al. 2010; Kusakabe et al. 2018). However, the largest sample of LAEs analyzed so far consists of 4400 LAEs over 19 deg^2 at $z = 2.2$ (Ono et al. 2021) combined from SILVERRUSH (Ouchi et al. 2018) and CHORUS (Inoue et al. 2020). Clustering analyses over areas of 0.25–1.6 deg^2 have also been performed at $z = 2.1$ (250 LAEs, Guaita et al. 2010), $z = 3.1$ (356 LAEs, Ouchi et al. 2010 and 162 LAEs, Gawiser et al. 2007), $z = 3.3$ (959 LAEs, Ono et al. 2021), $z = 4.5$ (151 LAEs, Kovač et al. 2007), and $z = 4.9$ (349 LAEs, Ono et al. 2021), $z = 5.7$ (2881 LAEs, Ouchi et al. 2018), and $z = 6.6$ (680 LAEs, Ouchi et al. 2018).

While previous clustering analyses have shown that LAEs are hosted by low-mass halos, the halo occupation fraction and detailed halo occupation distribution are still uncertain. The combination of larger area reducing cosmic variance (see Figure 5 in Kusakabe et al. 2018) and increased statistics reducing Poisson-like errors on correlation function measurement will allow us to improve the constraints on the bias of dark matter halos hosting LAEs and how it evolves with redshift. Following Ouchi et al. (2018), we can include halo occupation distribution parameters when modeling the observed angular correlation function to determine the fractional occupation of dark matter halos by LAEs as a function of the halo mass and the number of LAEs that are satellite galaxies in more massive halos.

2.4. Reconstructing the Expansion History of the Universe

The large-scale distribution of LAEs revealed by ODIN will provide a unique opportunity to measure the expansion history at $z > 2$, and hence test the standard model of cosmology. Recently found tensions between cosmological parameters inferred from early and late Universe data hint at new physics beyond the ΛCDM model, which could include departures from General Relativity or the presence of additional energy density components such as early dark energy. LSS surveys can be used to reconstruct the expansion history of the Universe by utilizing standard rulers or populations.

One example is the amplitude of the genus of the matter density. The genus is a member of the Minkowski Functionals and is a topological quantity that provides a measure of the connectivity of the matter distribution. The amplitude of the genus is relatively insensitive to redshift-dependent tracer bias and non-Gaussianities induced by gravitational collapse on quasi-linear $\sim\mathcal{O}(10$ Mpc) comoving scales. Hence, this statistic provides a relatively pure measurement of the connectivity of the initial state of the dark matter field and should be conserved with redshift to high accuracy $\sim\mathcal{O}(1\%)$ (Park & Kim 2010; Speare et al. 2015; Appleby et al. 2017, 2018). Spurious evolution in the genus amplitude would be observed if an incorrect cosmology is selected. Consequently, by measuring this quantity at different redshifts, one can determine the

distance–redshift relation that minimizes the evolution (Park & Kim 2010).

Another possibility is to use the shape of the two-point correlation function and apply the extended Alcock–Paczynski test (Park et al. 2019; Dong et al. 2023) to the ODIN data. As the shape of the two-point correlation function of cosmic objects is insensitive to the growth of structure and their bias, it is a good "standard shape" and can be used to measure the expansion history of the universe. Recently, the method has been applied to the low-redshift SDSS survey data, and a tight constraint on the dark energy equation of state parameter $w = -0.903 \pm 0.023$ was obtained for a flat wCDM universe, which is 4.2σ away from the ΛCDM model (Dong et al. 2023). The analysis can be applied to the higher redshift universe revealed by ODIN, to explore the possibility of potential nonstandard dark energy signatures, and more generally test if the observed universe is consistent with a decelerating epoch as predicted by the current standard cosmology.

ODIN will produce maps of LAEs at $z = 2.4$, 3.1, and 4.5 over large contiguous areas, which is ideal for studying LSS using these methods. Although we expect the LAE bias to be redshift-dependent due to selection effects and galaxy evolution, the genus amplitude should be practically insensitive to these artifacts. The genus of two-dimensional slices of the SDSS-III Baryon Oscillation Spectroscopic Survey (York et al. 2000) galaxy distribution at $z \sim 0.5$ has previously been measured (Appleby et al. 2017, 2021), and the genus extracted from the LAEs can be directly compared to these low-redshift results.

To perform this analysis, we must first understand how LAEs are biased relative to the underlying matter distribution. This can be determined using cosmological hydrodynamic simulations. Horizon Run 5 (HR5: Lee et al. 2021; Park et al. 2022) is a cosmological hydrodynamical simulation with a simulation box size of $\sim 1\ \mathrm{cGpc}^3$ and a high-resolution cuboid zoom-in region of $1049 \times 119 \times 127\ (\mathrm{cMpc})^3$, where the spatial resolution reaches down to ~ 1 kpc. The geometry of the zoom-in region is designed to be optimized for generating mock lightcone data for deep field surveys such as ODIN. Mock LAE data can be constructed using semi-analytic prescriptions, and the relation between LAEs and dark matter fields can be directly compared on quasi-linear scales using snapshot data from the simulation.

3. The ODIN Survey Design

3.1. ODIN Narrowband Filters

In Figure 1, we show the three ODIN narrowband filters made for the Dark Energy Camera. The same figure also shows the transmission curves for the broadband filters we use in conjunction to make LAE selections. These are the Subaru Hyper Suprime-Cam filters (*grizy*), the CFHT MegaCam *u*-band filter, and (in the near future) the LSST *ugrizy* filters. All data represent the total throughput including filter transmission, optics, detector, and mirror. The basic filter characteristics are summarized in Table 1 together with the expected redshift selection function of each filter, peaking at $z \approx 2.4$, 3.1, and 4.5, for the *N*419, *N*501, and *N*673 filters, respectively.

The ODIN filters are designed for dual use, i.e., to promote both high-redshift and Galactic science. The *N*501 filter can isolate [O III]λ5007 while avoiding [O III]λ4959. At zero velocity, the filter transmission at 4959 Å and 5007 Å is 10% and 99%, respectively. At $\Delta v = \pm 500\ \mathrm{km\ s^{-1}}$, the transmission changes to 5% (25%) and 97% (99%). Similarly, The *N*673 filter samples [S II] emission at $|v| \leqslant 500\ \mathrm{km\ s^{-1}}$ at a nearly constant transmission.

A combination of *N*673 and *N*501 can identify [O III] emitters at $z = 0.34$ masquerading as *N*673-detected LAEs (N. Firestone et al. 2023, in preparation) by simultaneously detecting [O II] emission with *N*501. For *N*501-detected LAEs at $z = 3.1$, *N*673 samples He II1640 emission to constrain their average stellar population properties via stacking analysis. For *N*673-detected LAEs at $z = 4.5$, Lyman continuum radiation that leaks out can be detected in the *N*501 filter.

All three filters are circular in shape with a diameter of 620 mm and are designed to have a transmission curve as close as possible to a top hat in shape. The post-production lab measurements were made in a parallel beam with 5° angle of incidence at the Asahi Spectra Ltd. facility on 49 points distributed along five concentric circles across the focal plane to characterize the variation of transmission. The expected transmission at normal incidence ($f/3.6$) is then computed based on these measurements. In Figure 2, we show the results at five different angular distances from the field center. As one moves farther away from the center of DECam's 1.°1 circular field, the central wavelength tends to shift blueward, and the transmission increasingly deviates from being top hat in shape.

The change in filter transmission as a function of the field position is expected to have a negligible impact on our science goals. As we discuss in Section 4.1, the dither patterns for most ODIN fields are designed to minimize transmission variations by observing the same objects at many locations within the focal plane. Doing so ensures that, throughout a given field, the effective transmission is as close as possible to a weighted average of the curves shown in Figure 2. Upon observational validation of these fluctuations, it may be possible to utilize the transmission variation to perform a single-filter "tomography" and determine a more precise redshift of bright LAEs (Zabl et al. 2016).

3.2. ODIN Survey Fields

The choice of ODIN fields is based primarily on the maximum depth of existing or future broadband imaging data, and in several cases, on the availability of spectroscopy. The seven ODIN fields include three of the Subaru Strategic Program deep fields, all five LSST Deep Drilling Fields (DDFs), two Euclid Deep Fields, and two fields with (nearly) full coverage of spectroscopic coverage from the Hobby-Eberly Telescope Dark Energy eXperiment (HETDEX). Together, these data sets will enable a wide range of scientific investigations on the properties of LAEs, the utility of LAEs as tracers of the LSS, and identification of protoclusters and their signposts (Section 2). The complete list of the ODIN survey fields and their characteristics are presented in Table 2 and the layout of each field is summarized in Figure 3.

Within a year after the LSST begins, five of the seven ODIN fields will have the deepest wide-field optical data available (Table 2), surpassing the current depths of the SSP Deep fields. Three of the SSP deep fields are also ODIN fields, namely, E-COSMOS, XMM-LSS, and Deep2-3, which are the priority fields for ODIN as they enable scientific investigations before the LSST begins. SHELA is one of the two fields being observed with a near 1:1 fill factor by the integral field spectrographs of HETDEX. Although SHELA is not part of

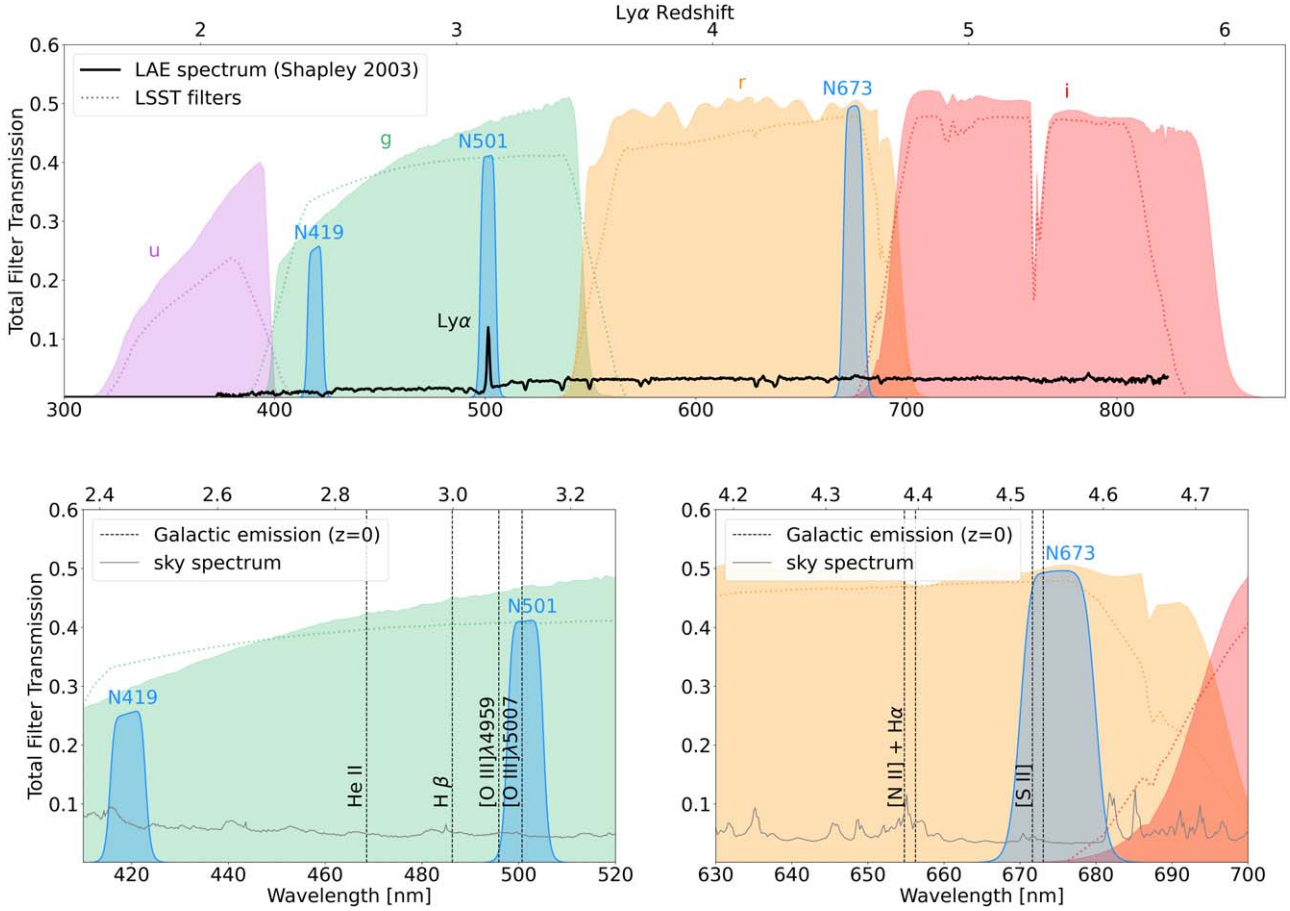

Figure 1. Top: ODIN narrowband filters made for DECam (blue shaded regions; from left to right, *N*419, *N*501, and *N*673, respectively) together with the transmission curves for the broadband filters from Subaru HSC (*gri*) and CFHT/MegaCam (*u*). Future LSST passbands for the same broad bands are shown as dotted lines. These imaging data are combined to isolate redshifted Lyα emission falling into the narrowband filters as illustrated by the template LAE spectrum (black) at $z = 3.1$. The Lyα redshift range is shown at the top. Bottom: zoom-in views of the three ODIN filters. Overlaid are strong Galactic emission lines (vertical dotted lines) and the sky spectrum (gray curves). *N*501 and *N*673 sample the [O III]λ5007 and [S II] emission from Galactic sources and nearby galaxies.

Table 1
Filter Summary

Filter	λ_C (nm)	λ_l[a] (nm)	λ_u[a] (nm)	FWHM (nm)	z_C	Δz
*N*419	419.3	415.54	423.01	7.46	2.449	0.061
*N*501	501.4	497.60	505.17	7.56	3.124	0.062
*N*673	675.0	670.01	680.03	10.02	4.553	0.082

Note.
[a] λ_l and λ_u give the endpoints of each filter's FWHM. z_C and Δz represent the central wavelength and the FWHM of each filter in redshift space, respectively.

any deep field imaging surveys, ODIN has been steadily improving on the BB depths in the area that offers continuous IRAC coverage.

3.3. Survey Parameters and Expectations

The ODIN survey parameters are optimized for the detection of protoclusters as LAE overdensities. The ability to detect protoclusters as medium-scale enhancements above the average field depends on a combination of two factors. First, a high surface LAE density, $\Sigma_{\rm LAE}$, improves the significance of protocluster detection by lowering the Poisson fluctuations associated with galaxy counts. Second, a smaller line-of-sight thickness ($d_{\rm los}$) minimizes the projection effects that typically suppress, but sometimes enhance, measured overdensities. To this end, the detection efficiency parameter $p_p \equiv \Sigma_{\rm LAE}/d_{\rm los}$ is kept relatively constant at all three ODIN redshifts. However, the DECam Exposure Time Calculator (ETC) suggested that achieving the same p_p level for *N*673 requires prohibitively large integration times (≈50% more than *N*419 and *N*501 time combined). We therefore choose a slightly lower p_p value to set the nominal depth for *N*673 observations.

While $d_{\rm los}$ is tied to the width of the filter transmission, the mean LAE surface density, $\Sigma_{\rm LAE}$, depends on the imaging depth. Because the broadband data typically extend $\gtrsim$1 mag deeper than our narrowband observations, $\Sigma_{\rm LAE}$ is primarily determined by the seeing and our narrowband filter exposure times. We estimate the LAE surface density at a fixed NB depth using field Lyα LFs (Gronwall et al. 2007; Ouchi et al. 2008; Ciardullo et al. 2012; Sobral et al. 2018) interpolated to the redshift corresponding to each narrowband filter's central wavelength. In this estimate, we assume that the Lyα luminosity dominates the narrowband flux density.

In Table 3, we list the nominal depths of our narrowband data and the corresponding Lyα flux and the surface brightness limits. The expected LAE surface density is computed using the standard threshold for LAE selection of rest-frame equivalent width >20 Å, which has been shown to avoid [O II] contamination at $\lambda \sim 5000$ Å (Gawiser et al. 2007; Gronwall et al. 2007). We also list the comoving line-of-sight

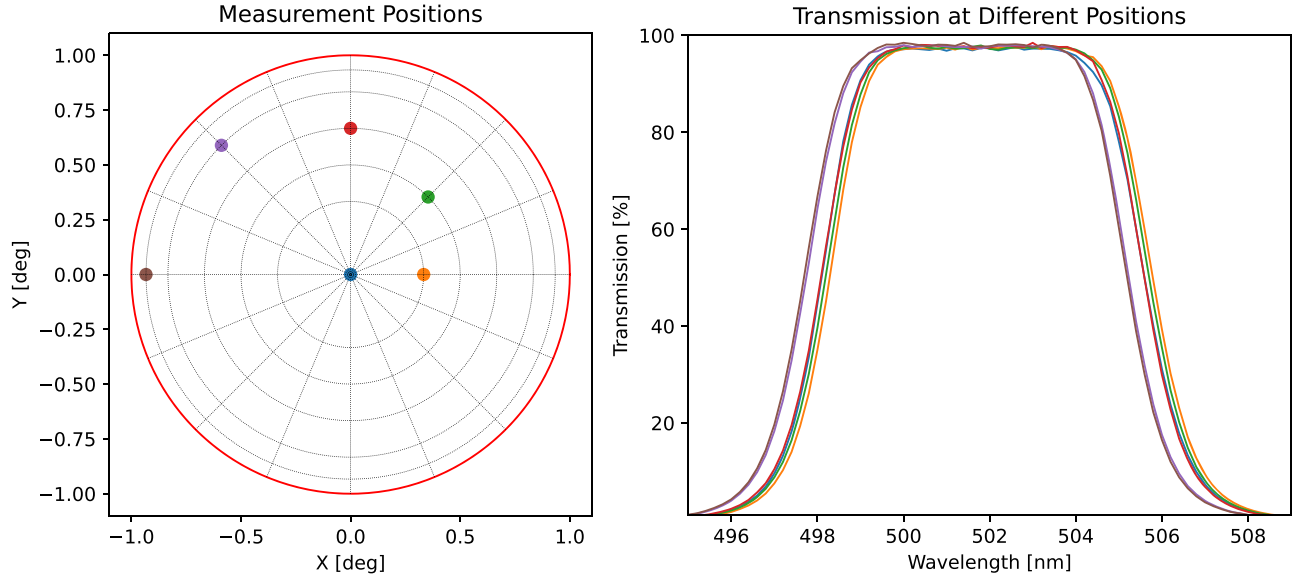

Figure 2. Left panel: the focal plane of DECam is shown as a red circle. Of the 49 positions at which the measurements were made, we only show the *N*501 filter transmission at the six positions indicated by the colored circles. Variations in the transmission curve are primarily a function of the distance from the center. Right panel: while the transmission curve shifts blueward by a few angstroms near the edge of the field, it remains relatively constant over the bulk of the DECam focal plane. The behavior of *N*419 and *N*673 filters is similar to that shown in this figure.

thickness, the comoving cosmic volume, and the protocluster detection efficiency (p_p). For the number of LAEs and the cosmic volume, we assume the full survey area of 91 deg^2. The expected number of protoclusters for each redshift slice is estimated based on this volume and the comoving number densities of clusters. As for the number densities of Coma- and Virgo-sized clusters (present-day masses of $\geqslant 10^{15} h^{-1} M_\odot$ and $(3\text{–}10) \times 10^{14} h^{-1} M_\odot$, respectively), we assume 1.84×10^{-7} and 2.48×10^{-6} cMpc^{-3}, respectively. These numbers are taken from the Millennium simulations-based (Springel et al. 2005) values computed by Chiang et al. (2013). The adopted cosmology for the simulation[26] is only slightly different from ours and we do not make any additional corrections. The uncertainty due to Poisson shot noise and cosmic variances are expected to be larger than the changes from different cosmologies, particularly for the Coma progenitors.

As for the expected number of LABs, we assume a constant density across all redshifts. The number density estimate for bright and extended LABs ($L_{\mathrm{Ly}\alpha} \gtrsim 1.5 \times 10^{43}$ erg s^{-1}, $A_{\mathrm{iso}} \geqslant 16$ arcsec^2: Yang et al. 2010) is $1.0^{+1.8}_{-0.6} \times 10^{-5}$ cMpc^{-3} adopting a cosmology with $\Omega_m = 0.3$, $\Omega_\Lambda = 0.7$, and $h = 0.7$. The uncertainties reflect strong field-to-field variations as well as the uncertainties originating from shot noise for a small-area (1.2 deg^2) survey. The values listed in Table 3 are corrected for the difference in cosmology which is at a ≈10% level. Recently, from the ODIN COSMOS/*N*501 data, Ramakrishnan et al. (2023) reported 129 LABs over a ≈9 deg^2 region, forecasting that the total number of LABs may be closer to the upper limit in the table. More stringent limits will be placed by combining the LAB samples in multiple fields (B. H. Moon et al. 2023, in preparation).

In Figure 4, we illustrate how massive structures may appear at the nominal p_p range adopted by ODIN. Using the IllustrisTNG simulation suite (Weinberger et al. 2017), we first choose three massive structures. In terms of $M_{z=0}$, the total mass at $z = 0$, they are ranked #1, #2, and #7, respectively. The dark matter distribution of these structures at $z = 3$ is shown in the left panels. To match the survey parameters, we create a (60 cMpc)^3 volume centered on the progenitor of each cluster at $z = 3$. Adopting a minimum stellar mass of $M_{\mathrm{star}} = 10^9 M_\odot$ to match the LAE clustering measurements from the literature (Gawiser et al. 2007; Kovač et al. 2007; Guaita et al. 2010; Kusakabe et al. 2018), we randomly select a subset of halos above the threshold that matches the ODIN surface densities (Table 3). The surface density map is then created by smoothing the "LAE" distribution with a fixed kernel. We choose a two-dimensional Gaussian kernel with a FWHM of 5.″2 (10 cMpc at $z = 3$), comparable to the expected size of a protocluster. We note that, as a simple demonstration, we use the $z = 3$ matter distribution in these structures to simulate the LAE maps at all three ODIN redshifts by simply matching the respective LAE surface densities.

Figure 4 demonstrates that ODIN is expected to detect Virgo- or Coma progenitors with ease provided that LAEs represent an unbiased tracer of low-mass halos. While we chose to use a random subset of halos as mock LAEs, more realistic modelings of LAEs following the recipes of Weinberger et al. (2019) or Mason et al. (2018) do not meaningfully alter the result (Lee et al. 2024; M. Andrews et al. 2023, in preparation; S. Im et al. 2023, in preparation). However, reality may be more complicated. Radiative transfer effects could cause LAEs to avoid the regions of highest density (e.g., see Momose et al. 2021; Huang et al. 2022). Additionally, as galaxies grow more massive, star formation activity is expected to ramp up and produce more interstellar dust, lowering their likelihood of being classified as LAEs (e.g., Weiss et al. 2021). These considerations suggest that the densest and most evolved regions may not be represented as the highest LAE overdensities. More observational evidence is needed to firmly establish the level of this potential bias.

In Figure 5, we show the areal coverage versus depths of existing narrowband z = 2–5 Lyα surveys along with the ODIN survey. These studies include the combined results from

[26] The cosmological parameters assumed for the Millennium Run is $\Omega_m = 0.25$, $\Omega_\Lambda = 0.75$, $h = 0.73$, $\sigma_8 = 0.9$.

Table 2
Summary of ODIN Fields and Available Data

Field	Field Center (J2000)	Area (deg^2)	Pointing Pattern	Notable Facts
ELAIS-S1	9.°45, −44.°00	10	Two Rings	DDF
SHELA[a]	20.°5, 0.°00	24	Spiral	HETDEX, DESI access
XMM-LSS	35.°71, −4.°75	10	Two Rings	DDF, SSP, DESI access
CDF-S	53.°13, −28.°10	10	Two Rings	DDF, EDF
EDF-Sa[b]	58.°90, −49.°32	10	Two Rings	EDF, DDF, SPHEREx DF
EDF-Sb[b]	63.°60, −47.°60	10	Two Rings	EDF, DDF, SPHEREx DF
E-COSMOS	150.°10, 2.°18	10	Two Rings	DDF, SSP, DESI access
Deep2-3	352.°1, −0.°28	7	Spiral	SSP, DESI access
Total	⋯	91		

Survey	BB Filters		5σ Point Source Sensitivity
SSP Deep[c]	*ugrizy*	⋯	27.1, 27.5, 27.1, 26.8, 26.3, 25.3
LSST DDF Y1	*ugrizy*	⋯	26.7, 27.9, 28.1, 27.4, 26.6, 25.3
LSST DDF Y10	*ugrizy*	⋯	28.0, 29.2, 29.4, 28.7, 27.9, 26.6
LSST Y3	*ugrizy*	⋯	25.6, 26.8, 27.0, 26.3, 25.5, 24.2
LSST Y10	*ugrizy*	⋯	26.3, 27.5, 27.7, 27.0, 26.2, 24.9

Notes.
[a] For SHELA, we give the RA range instead of the pointing center. SHELA is approximately 12° wide in the east–west direction.
[b] The Euclid Deep Field South (EDF-S) field has recently been designated as the fifth LSST Deep Drilling Field. It will be covered by two slightly overlapping pointings ("EDF-Sa" and "EDF-Sb"), the coordinates of which are listed separately.
[c] SSP Deep field sensitivities include those of the Subaru HSC data and of the CLAUDS *u*-band data from CFHT MegaCam (Sawicki et al. 2019). DDF: LSST Deep Drilling Field (https://www.lsst.org/scientists/survey-design/ddf); SSP: Hyper Suprime-Cam Subaru Strategic Plan (https://hsc.mtk.nao.ac.jp/ssp/survey); EDF: Euclid Deep Field (https://www.cosmos.esa.int/web/euclid/euclid-survey); HETDEX: the Hobby-Eberly Telescope Dark Energy eXperiment (https://hetdex.org); SPHEREx (https://spherex.caltech.edu/).

the SILVERRUSH and CHORUS conducted with Subaru/HSC (Ono et al. 2021; Kikuta et al. 2023) as well as several earlier measurements with Subaru/Suprime-Cam (Ouchi et al. 2008; Prescott et al. 2008) and Mayall/Mosaic3 (Malavasi et al. 2021).

4. Observations and Data Reduction

4.1. Dither Patterns

DECam images a circular region of 2.°1 in diameter. In comparison, the LSST field of view (FOV) is 3.°5 in diameter. To achieve a reasonable level of uniformity across the five LSST DDFs using DECam, we designed a two-ring dither scheme as illustrated in the top left panel of Figure 6. DECam pointings are positioned along two concentric rings with radii 1.°0 and 1.°6 from the field center.[27] The number of visits in each ring is determined based on the 1200 s exposure time per frame and the effective exposure time per pixel needed to reach the target depths as discussed in Section 4.2. The radii and total exposure time ratio of the rings are calibrated to minimize the variation of the depths in the radial direction by controlling the degree of overlap between the inner- and outer-ring exposures.

In the top right panel of Figure 6, we show the nominal exposure time map for the *N*419 observations in COSMOS. The final map is similar to this figure except for the presence of satellite trails. Each sky location within the LSST Deep Drilling Field gets observed by at least 10 pointings, naturally filling in chip gaps to yield locally uniform depth. The angular spacing between adjacent pointings in a given ring is smaller for the *N*501 and *N*673 observations because the exposure time per pixel is higher, but adheres to the same principle. The exposure maps of all DDF fields in all filters are expected to be similar to that shown in the figure.

In a given ring, we randomly shuffle the order in which pointings are observed to ensure uniformity in seeing across the field. We typically complete the inner ring pointings before starting the outer ring to enable early science. For the EDF-S, which is composed of two slightly overlapping LSST pointings, we randomly select pointings from rings in both EDFS-a and EDFS-b, as the CTIO 4 m slew time from one to the other is never much larger than the DECam readout time.

For the fields that are not DDFs, namely, SHELA and Deep2-3, we take a different approach. For SHELA, we match the NB coverage as closely as possible to the existing BB data (Wold et al. 2019). The coverage is comprised of eight DECam pointings that follow a spiral pattern with small dithers to fill gaps, as shown in Figure 3. On the other hand, Deep2-3 is defined via four overlapping HSC pointings. In both SHELA and Deep2-3, we employ a spiral dither pattern. As illustrated in the bottom left panel of Figure 6, dither positions move away from the pointing center along a spiral by a small offset each time such that chip gaps along the R.A. and decl. axes never repeat, yielding an X-shaped pattern designed to fill the CCD gaps and to cover the BB regions with uniform coverage. In all narrowband filters, we use the identical pattern repeating it as many times as needed to achieve the target depth.

4.2. ODIN Data Acquisition and Reduction

The ODIN survey began its observations in 2021 February. At the time of this article, the survey is ≈50% complete. A comprehensive summary of the LAE selection will be given

[27] Although this is being described as a dither pattern consisting of two rings of large dithers without ever using the central pointing, it could equally well be described as a two-ring pointing pattern with no dithers performed.

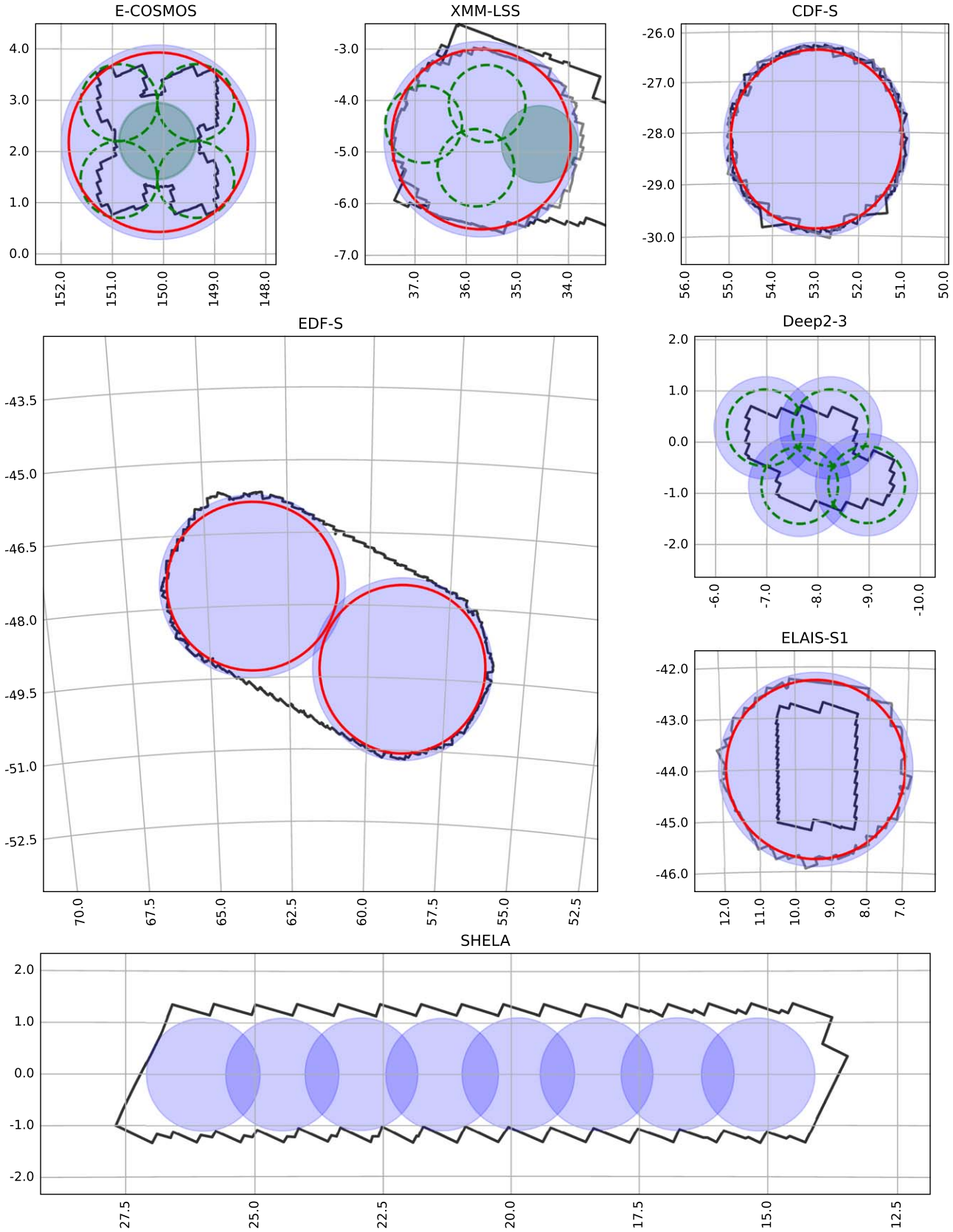

Figure 3. Layout of the seven ODIN fields. Blue shades indicate the area covered by ODIN at ⩾70% of the target depths. Red circles mark the LSST field of view. Green solid (dashed) circles denote the SSP ultradeep (deep) regions. All seven fields will receive LSST coverage. The existing Spitzer IRAC coverage from the DeepDrill program is outlined in light gray while other available data are shown in black.

Table 3
Expectations for the ODIN Survey

	*N*419	*N*501	*N*673	Total
Redshift	2.45 ± 0.03	3.12 ± 0.03	4.55 ± 0.04	⋯
Exp. Time [hr]	6.0	5.0	9.0	⋯
5σ depth[a] [mag]	25.5	25.7	25.9	⋯
5σ Line Flux [cgs[b]]	3.1×10^{-17}	1.8×10^{-17}	1.1×10^{-17}	⋯
SB limit [cgs[b]]	3.5×10^{-18}	2.1×10^{-18}	1.2×10^{-18}	⋯
Line-of-sight thickness [cMpc]	76.0	57.0	50.6	⋯
Cosmic Volume [cMpc^3]	7.43×10^7	7.04×10^7	8.50×10^7	2.30×10^8
LAE density [arcmin^{-2}]	0.19	0.17	0.10	0.46
Protocluster selection efficiency, p_p	1.1×10^{-3}	1.3×10^{-3}	0.8×10^{-3}	⋯
# of LAEs	60,000	50,000	30,000	140,000
# of protoclusters[c]	13.7 (184.3)	13.0 (174.6)	15.6 (210.8)	42.3 (569.7)
# of LABs	268–1874	254–1775	308–2154	≈800–5800

Notes.
[a] The limiting magnitudes are computed within 2″ diameter apertures assuming 1.″2, with seeing (and aperture) scaled with wavelength as predicted in the DECam ETC. We have assumed an average sky brightness corresponding to 0, 3, and 3 days from new moon for *N*419, *N*501, and *N*673, respectively.
[b] Line fluxes and surface brightness limits are given in units of erg s^{-1} cm^{-2} and erg s^{-1} cm^{-2} arcsec^{-2}.
[c] The number of Coma (Virgo) analogs expected within the survey volume.

elsewhere (N. Firestone et al. 2023, in preparation), and here we focus on the general practice adopted for our observations and data processing.

ODIN observations of all filters use an exposure time of 1200 s, which is motivated by two considerations: the low sky background expected in narrowband filters requires that our exposure times be long enough to ensure that the 7 e$^-$ read noise of the DECam CCDs is not a dominant factor. According to the DECam exposure time calculator, in a 1200 s exposure in *N*419, *N*501, and *N*673, the fraction of readout noise is ≈30%, 13%, and 4% of the sky background noise measured in a 2″ diameter circular aperture at new moon. A countervailing need is to avoid filling too much of the detector with cosmic rays, which, given the thick CCDs on DECam, can be highly extended and morphologically complex. This drives us to set a maximum exposure time of 1200 s.

During our observations, we utilize the *copilot* software (Burleigh et al. 2020), a tool developed for DECam to monitor observing conditions and image weight. Using the Pan-STARRS-1 photometric catalog (Schlafly et al. 2012), copilot measures seeing, transparency (T), and sky brightness (B). Based on these data, we compute relative image weights, w, as:

$$w \propto \frac{T^2\,\mathtt{exptime}^2}{B\,\mathtt{seeing}^2}. \quad (1)$$

The weight is normalized by values expected in a nominal dark sky condition. For (*N*419, *N*501, *N*673) a weight of unity would be achieved in a 1200 s exposure with $T = 1$, seeing of (1.2, 1.1, 1.0)″ and a background level of (50, 100, 200) ADU per pixel. The primary goal is to ensure that each designated pointing receives a combined weight of ≈1 by the completion of our observations. In practice, this means that the same pointing can be revisited to add more depth until the combined weight is similar to the original specification. The weighting scheme given in Equation (1) can accommodate shorter-exposure frames as long as readout noise remains subdominant.

We process and stack the ODIN data using the DECam Community Pipeline (CP: Valdes et al. 2014; Valdes 2021) as follows. Each DECam exposure consisting of data from the 60 calibrateable CCDs is flat-fielded separately by dome flats, star flats, and dark sky illumination flats. Dark sky illumination flats are created by coadding unregistered stacks of exposures. Dome flats are produced by stacking sequences of 11 exposures taken each night; star flats are made from widely dithered exposures of a star field using the algorithm of Bernstein et al. (2017).

For each CCD, the background is measured by the modes of pixel values in small blocks with sources masked. Blocks with an insufficient number of background pixels are replaced by interpolation from nearby blocks. A spline surface is fit to the modes. In fields with prominent reflections from very bright stars, the modes are used directly to best handle the fine structure of the ghosts. The background is subtracted while maintaining the mean. The block size chosen to measure the background is sufficiently large to ensure that it does not introduce any photometric bias for extragalactic sources; however, as the size is smaller than the region affected by bright stars, the procedure can lead to over-subtraction of the faint halos.

The CP provides a data quality flag for every pixel for every exposure. The flags, in order of precedence, are known bad CCD pixels, saturated or bleed trail pixels, and cosmic ray and streak identifications. The last analysis is done on individual exposures but multiple ODIN exposures allow for further identification via transient signals. In addition, the ODIN team produces satellite trail masks for affected exposures which are combined with the CP data quality masks. The pixels flagged in the master quality mask are excluded from consideration when coadding all the exposures to create the deep image stacks.

An astrometric solution is derived for each CCD by matching stars to Gaia-EDR3 (Gaia Collaboration et al. 2021). While the higher order distortions are predetermined and fixed, the low order terms are updated using the astrometric solver SCAMP (Bertin 2006) with continuity constraints between CCDs. The rms of a plate solution is typically a few hundredths of an arcsecond. We reproject the exposures to a standard tangent plane sampling at the pixel scale of 0.″27 pix^{-1} using sinc interpolation. A fixed tangent point is used for all the exposures in a given field with the exception of

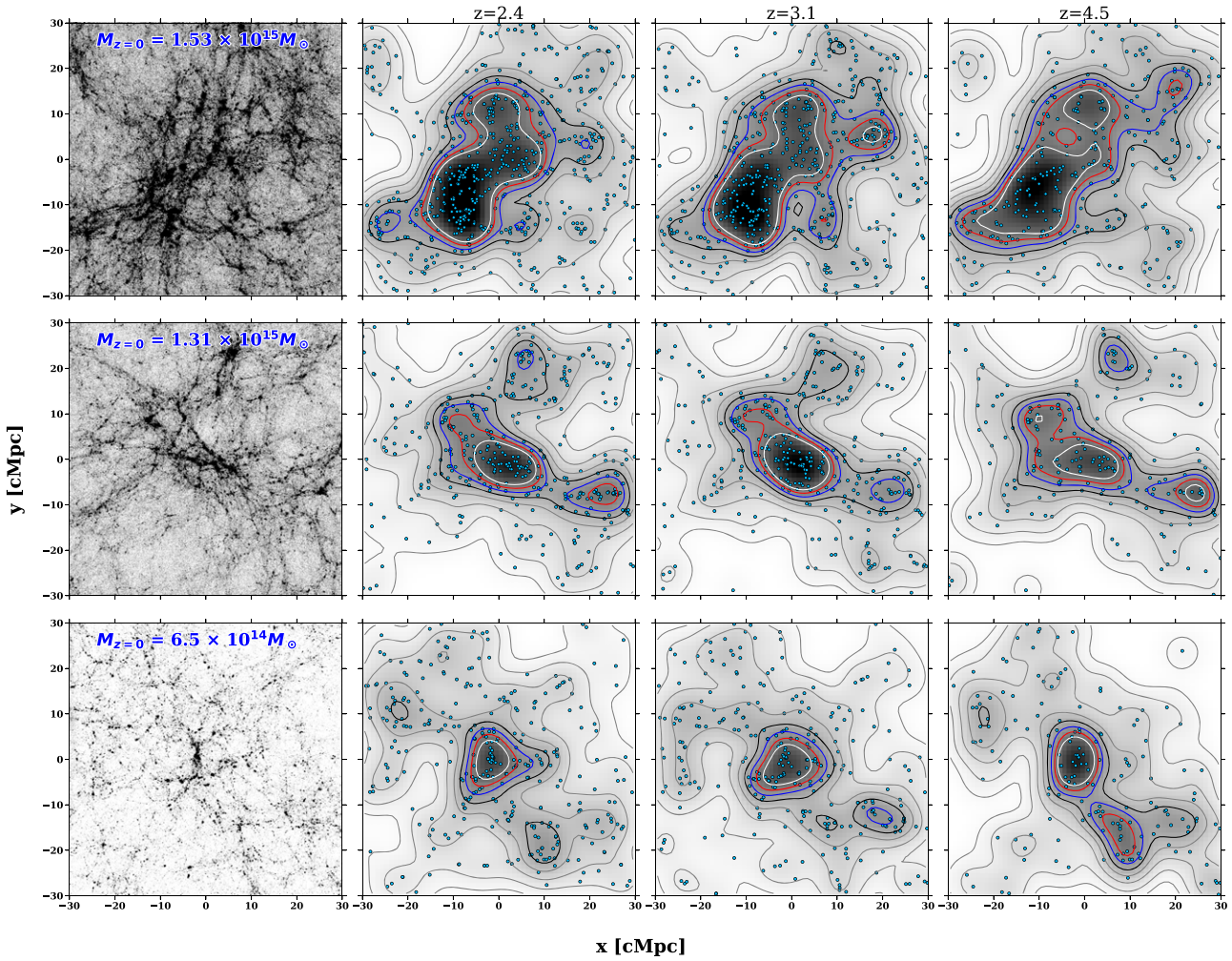

Figure 4. On the leftmost column, we show the dark matter distribution at $z = 3$ around three present-day cosmic structures identified in the IllustrisTNG TNG300 simulation. In all cases, the line-of-sight thickness is 60 cMpc, roughly matched to the ODIN survey. The present-day masses are also indicated. Of the halos hosting galaxies with stellar mass $M_{\rm star} \geqslant 10^9 M_\odot$, we randomly assign a subset as "LAEs" to match the expected field LAE surface density at $z = 2.4$, 3.1, and 4.5. The mass threshold is chosen to reproduce the observed LAE clustering strengths. The second, third, and fourth columns show the positions of these mock LAEs together with the Gaussian-kernel-smoothed density maps. The white, red, blue, and black lines denote 5σ, 4σ, 3σ, and 2σ iso-surface-density contours, respectively. These images build clear expectations of how LAEs can trace massive cosmic structures at high redshift.

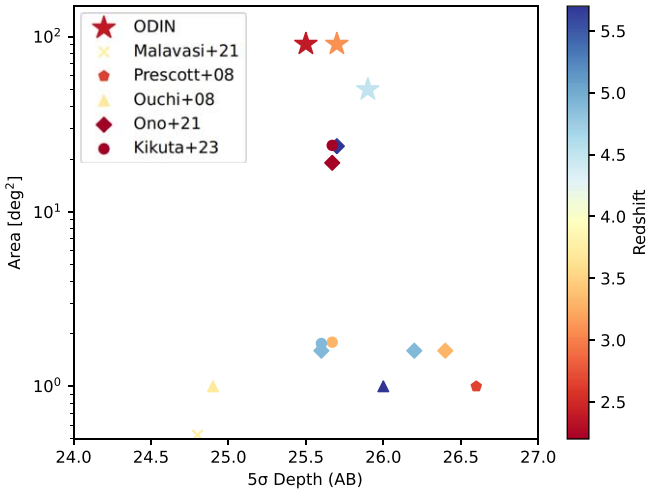

Figure 5. Comparison of the imaging depth and area coverage of recent surveys with ODIN (stars). All data are color coded by redshift. Diamonds and circles represent the combined SILVERRUSH and CHORUS surveys (Ono et al. 2021; Kikuta et al. 2023). Earlier surveys with Subaru/Suprime-Cam (Ouchi et al. 2008; Prescott et al. 2008, triangles and pentagon, respectively), Mayall/Mosaic (Malavasi et al. 2021, cross) are also listed.

the two largest ODIN fields which are more than 10° across. For EDF-S and SHELA, two and four separate tangent points are used.

Individual exposures are matched to the Pan-STARRS-1 photometric catalog (Schlafly et al. 2012) to determine a zero-point (`magzero`) and a photometric depth in magnitude (`depth`). The latter is computed as:

$$\texttt{depth} = \texttt{magzero} - 2.5 \log\left(5\sigma\sqrt{\pi r_{\rm op}^2}\right), \qquad (2)$$

where σ is the pixelwise sky noise and $r_{\rm op}$ represents the size of an optimal aperture (for a pure Gaussian seeing) whose diameter is 1.35 times the measured seeing FWHM. The `magzero` parameter combines sky transparency and exposure time for a given frame while `depth` represents the 5σ uncertainty. The `depth` parameter is then converted to linear relative counts and squared to form a normalized relative weight for each frame. All exposures are coadded as a weighted mean with statistical rejection (constrained sigma clipping) of outliers to remove the large number of cosmic rays accumulated in our long exposures.

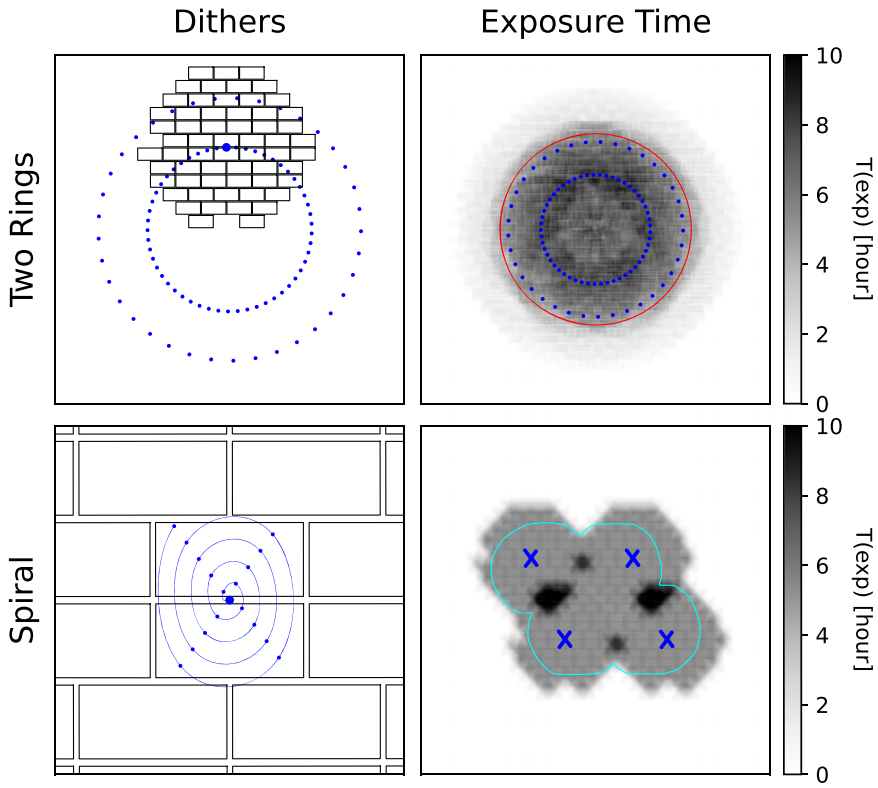

Figure 6. Two dither patterns used for the ODIN survey. Top left: blue points mark the center position of each DECam pointing in the two-ring dither pattern. The radius of the inner and the outer ring is 1.°0 and 1.°6, respectively. The individual CCDs of DECam are shown in black. Top right: resultant exposure map for *N*419 together with the pointing centers (blue points) and the LSST field of view (red circle). Bottom left: the spiral dither positions are overlaid on the center of the DECam focal plane, with individual CCDs shown in black. Small dithers along the spiral create an X-shaped set of pointings that enable uniform coverage by minimizing the overlap between chip gaps. Bottom right: the exposure map for *N*419 of the Deep2-3 field employs the spiral dither pattern of four overlapping fields. The pointing centers are shown in blue. The broadband coverage from SSP is shown in cyan.

In Figure 7, we show the full-depth mosaic of CDF-S in *N*501 overlaid with the LSST FOV (yellow circle) and the size of the Moon. Similar to the SSP data release, the ODIN stack is split into multiple "tracts," each $1.^{\circ}7 \times 1.^{\circ}7$ in size with an overlap of $1'$ for the ease of data handling. The only exception to this convention is SHELA, for which we create four separate stacks each of which contains two adjacent DECam pointings.

The ODIN observations began in 2021 February, with the top priorities given to the SSP Deep Fields where deep broadband data already exists. At the time of writing, COSMOS and XMM-LSS are complete with all three NB filters, while Deep2-3 is complete with *N*419 and *N*501. As for SHELA, EDF-S, and CDF-S, each has been imaged with two filters with varying degrees of completion. ELAIS-S1 remains the only field which we have not yet observed. Nominally, the NOIRLab survey time is expected to end by the 2024B observing semester, pending weather conditions and survey completion rate at the time. The public data release will follow within a year after the survey concludes, and will include the full mosaicked imaging data (both NB and BB), multi-wavelength photometric catalogs, as well as the lists of LAE- and protocluster candidates identified by ODIN.

5. External Data

5.1. Broadband Optical Data

The detection of high-redshift LAEs requires that the ODIN narrowband data be compared existing broadband frames. For the Deep2-3, E-COSMOS, and XMM-LSS fields, these data come from the HSC SSP program (Aihara et al. 2018). In particular, we use the publicly available frames from the third data release (Aihara et al. 2022). Similar to that described in Section 4.2, we reproject the data using the common tangent point at the pixel scale of $0.''27\,\mathrm{pix}^{-1}$.

In the SHELA field, we use the archival DECam data taken as part of several NOIRLab programs. As described in Wold et al. (2019), the existing observations are composed of eight overlapping DECam pointings. We reprocess the data using the DECam CP and find that the depths vary significantly across the field. Since Fall 2021, ODIN has been conducting additional DECam imaging with the primary goal of homogenizing the sensitivity of broadband data with the top priority on the *gr* bands to enable a uniform selection of LAEs.

In the remaining three fields (EDF-Sab, ELAIS-S1, and CDF-S), the availability of the BB data across the $\sim$10 deg^2 field is currently limited. A subsection of CDF-S was observed repeatedly as one of the Dark Energy Survey deep fields (Hartley et al. 2022) designed to detect supernovae. While the approximate depths of these data are listed in Table 2, the sensitivity will be easily surpassed in 2026 by Rubin with uniform coverage within the ODIN fields. These considerations have been taken into account in setting the observational priorities.

5.2. Spitzer IRAC Data

All seven ODIN fields have existing Spitzer IRAC images which cover a substantial fraction of the survey area at depths that are useful for selecting massive galaxies in the ODIN

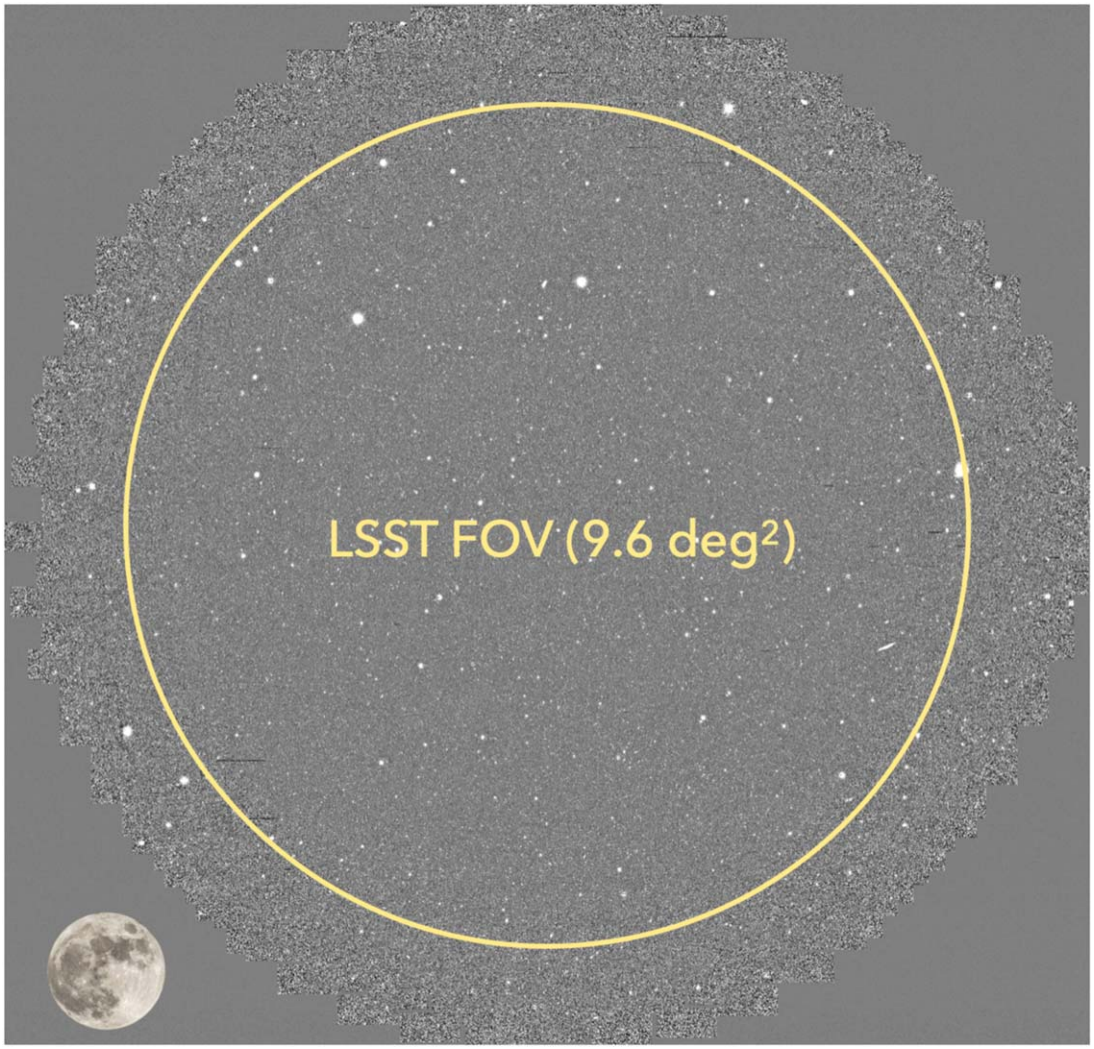

Figure 7. Final mosaic of CDF-S in *N*501. The yellow circle marks the position and area coverage of the planned LSST observations of CDF-S in *ugrizy* at the DDF depths indicated in Table 2. The to-scale size of the Moon is shown at the bottom left corner.

redshift range. These data sets will enable statistical association of massive galaxies with cosmic structures and/or LABs and elucidate the early formation histories of massive cluster ellipticals. The IRAC coverage of the ODIN fields is indicated by gray lines in Figure 3. Here, we briefly summarize the publicly available data.

The COSMIC DAWN survey obtained IRAC imaging of three Euclid Deep Fields (Euclid Collaboration et al. 2022). In all cases, we quote the 5σ detection limit, which is $\approx$0.5 μJy for EDF-N and CDF-S (i.e., the Euclid Deep Field Fornax) and $\approx$1.0 μJy for EDF-S. Additionally, Cosmic Dawn re-reduced all existing IRAC data sets in other Euclid calibration fields including XMM-LSS and COSMOS (both at $\approx$1.0 μJy) in a consistent manner. Smaller subsections of COSMOS, XMM-LSS, and CDF-S have also been imaged to varying depths by other programs. For a summary of the depths and areal coverage, we refer interested readers to Euclid Collaboration et al. (2022).

The DeepDrill survey imaged the full extent of three of the LSST DDFs, ELAIS-S1, XMM-LSS, and CDF-S with IRAC (Lacy et al. 2021), expanding the coverage of the Spitzer Extragalactic Representative Volume Survey (SERVS; Mauduit et al. 2012) at a comparable depth of $\approx$2 μJy (5σ). A larger section of ELAIS-S1 is imaged at a shallower depth ($\approx$3 μJy) by the Spitzer Wide-area InfraRed Extragalactic survey (Lonsdale et al. 2003). Deep2-3 is covered by both SERVS and the Spitzer coverage of HSC-Deep with IRAC for Z (SHIRAZ; Annunziatella et al. 2023) survey, where the depth of the latter is $\approx$1 μJy. Finally, the imaging of the SHELA was performed by the SHELA survey (Papovich et al. 2016) at the shallowest depth (5.5 μJy), which corresponds to a star-forming galaxy of moderate dust reddening, $E(B-V)=0.25$ and stellar mass of $\approx 10^{10.2} M_{\odot}$ at $z=2.5$.

5.3. Spectroscopy

Multiple ongoing spectroscopic programs are targeting ODIN-selected galaxies with DESI, Gemini GMOS, Keck DEIMOS, and the Prime Focus Imaging Spectrograph on the South African Large Telescope. These data have been highly successful in validating LAE selection, measuring the spatial structure of several protoclusters, and spectroscopically confirming more than 40 LABs. Presently, the number of ODIN LAEs with spectroscopic follow-up is $\approx$8000, 3000, and 800 at $z=2.4$, 3.1, and 4.5, respectively. The results from these programs will be presented in forthcoming papers.

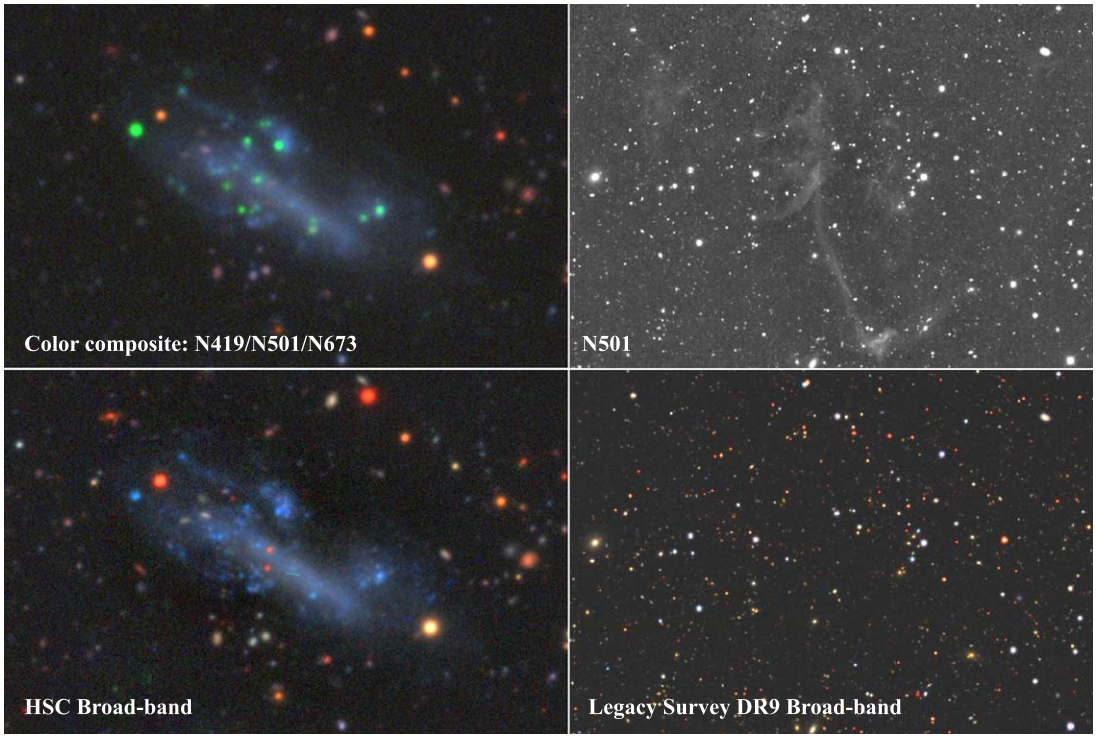

Figure 8. Left panels: a color-composite image of a nearby star-forming galaxy is displayed using the ODIN NB filters (top) and the HSC broadband filters (bottom). Star-forming knots are clearly delineated in the former in green as *N*501 samples O III nebular emission. Right panels: extended large-scale features, visible in the *N*501 image (top), likely trace shocked, [O III]-emitting gas associated with a planetary nebula, NGC 1360 located outside the ODIN field.

6. Ancillary Science

The deep NB data taken as part of ODIN can be used for a number of programs. These data can be visualized from the ODIN Legacy Viewer[28] where users can browse each stacked ODIN narrowband image as well as a color-composite frame that combines the ODIN NB data together.

The left panels of Figure 8 show a nearby star-forming galaxy located at $(\alpha, \delta) = (149.^{\circ}620, +1.^{\circ}694)$. The colors are computed from ODIN data (top) and HSC broadband images (bottom). Star-forming knots with strong [O III] emission are clearly delineated as green features in the top panel. The right panels show a small section in CDF-S centered on $(\alpha, \delta) = (53.^{\circ}164, -26.^{\circ}219)$ observed in *N*501 (top right) with Legacy Survey DR9 broadband data (bottom right). The complex and very extended [O III] emission feature likely originates from shocked gas associated with NGC 1360, a planetary nebula located at $(\alpha, \delta) = (53.^{\circ}311, -25.^{\circ}870)$, $\approx 20'$ northeast and outside the ODIN field. In the legacy viewer,[29] the gas is captured in the broadband data but only very close to NGC 1360. The sensitivity of the *N*501 and *N*673 data afforded by ODIN provides a unique opportunity to explore faint gaseous components of our Galaxy and star-forming regions of the nearby universe (e.g., Drechsler et al. 2023).

7. Summary

The ODIN collaboration is currently conducting a narrow-band survey with the largest area, covering ≈ 90 deg^2 with three custom filters down to depths of 25.5–25.9 AB. By sampling redshifted Lyα emission at $z = 2.4$, 3.1, and 4.5 in narrow cosmic slices (≈ 60 cMpc in thickness) within a 0.25 cGpc^3 volume, ODIN will enable robust measurements of the epochs' LSS by mapping out knots, groups, filaments, and cosmic voids within the underlying matter distribution using low-mass, Lyα-emitting galaxies.

ODIN will discover hundreds of distant protoclusters and thousands of the largest and most luminous Lyα nebulae, allowing us to study the physical association of these two rare types of cosmic objects and their relationships to the surrounding LSS. Through measurements of the LAE luminosity functions, SED, and clustering, we will determine the physical properties of these objects and their association with dark matter halos and obtain quantitative measurements of how LSS influences galaxy formation. The models of expansion history will be explored through measurements across cosmic time.

With Rubin, Euclid, and Roman on the horizon, the ODIN fields will become the deepest fields rich with spectroscopic and imaging data. When combined with these data, the ODIN data will have a lasting legacy in advancing studies of not only galaxy evolution at high redshift but also the Galaxy and the nearby universe.

[28] https://odin.legacysurvey.org/
[29] https://legacysurvey.org

Acknowledgments

This project used data obtained with the Dark Energy Camera (DECam), which was constructed by the Dark Energy Survey (DES) collaboration. Funding for the DES Projects has been provided by the US Department of Energy, the US National Science Foundation, the Ministry of Science and Education of Spain, the Science and Technology Facilities Council of the United Kingdom, the Higher Education Funding Council for England, the National Center for Supercomputing

Applications at the University of Illinois at Urbana-Champaign, the Kavli Institute for Cosmological Physics at the University of Chicago, Center for Cosmology and Astro-Particle Physics at the Ohio State University, the Mitchell Institute for Fundamental Physics and Astronomy at Texas A&M University, Financiadora de Estudos e Projetos, Fundação Carlos Chagas Filho de Amparo á Pesquisa do Estado do Rio de Janeiro, Conselho Nacional de Desenvolvimento Científico e Tecnológico and the Ministério da Ciência, Tecnologia e Inovação, the Deutsche Forschungsgemeinschaft and the Collaborating Institutions in the Dark Energy Survey.

The Collaborating Institutions are Argonne National Laboratory, the University of California at Santa Cruz, the University of Cambridge, Centro de Investigaciones Enérgeticas, Medioambientales y Tecnológicas-Madrid, the University of Chicago, University College London, the DES-Brazil Consortium, the University of Edinburgh, the Eidgenössische Technische Hochschule (ETH) Zürich, Fermi National Accelerator Laboratory, the University of Illinois at Urbana-Champaign, the Institut de Ciéncies de l'Espai (IEEC/CSIC), the Institut de Física d'Altes Energies, Lawrence Berkeley National Laboratory, the Ludwig-Maximilians Universität München and the associated Excellence Cluster Universe, the University of Michigan, NSF's NOIRLab, the University of Nottingham, the Ohio State University, the OzDES Membership Consortium, the University of Pennsylvania, the University of Portsmouth, SLAC National Accelerator Laboratory, Stanford University, the University of Sussex, and Texas A&M University.

Based on observations at Cerro Tololo Inter-American Observatory, NSF's NOIRLab (NOIRLab Prop. ID 2020B-0201; PI: K.-S. Lee), which is managed by the Association of Universities for Research in Astronomy (AURA) under a cooperative agreement with the National Science Foundation.

K.S.L. and V.R. acknowledge financial support from the National Science Foundation under grant No. AST-2206705 and from the Ross-Lynn Purdue Research Foundation Grant. This material is based upon work supported by the National Science Foundation Graduate Research Fellowship Program under grant No. 2233066 to N.F.. N.F. and E.G. acknowledge financial support from the National Science Foundation under grant No. AST-2206222 and from the NASA Astrophysics Data Analysis Program grant 80NSSC22K0487. H.S. acknowledges the support of the National Research Foundation of Korea grant, No. 2022R1A4A3031306, funded by the Korean government (MSIT). L.G., J.N., and A.S. acknowledge recognition from Fondecyt Regular No. 1230591, and J.N. acknowledges support from Universidad Andrés Bello grant No. DI-07-22/REG.

ORCID iDs

Kyoung-Soo Lee https://orcid.org/0000-0003-3004-9596
Eric Gawiser https://orcid.org/0000-0003-1530-8713
Changbom Park https://orcid.org/0000-0001-9521-6397
Yujin Yang https://orcid.org/0000-0003-3078-2763
Francisco Valdes https://orcid.org/0000-0001-5567-1301
Dustin Lang https://orcid.org/0000-0002-1172-0754
Vandana Ramakrishnan https://orcid.org/0000-0002-9176-7252
Byeongha Moon https://orcid.org/0009-0008-4022-3870
Nicole Firestone https://orcid.org/0000-0002-9811-2443
Stephen Appleby https://orcid.org/0000-0001-8227-9516
Maria Celeste Artale https://orcid.org/0000-0003-0570-785X
Moira Andrews https://orcid.org/0000-0002-1895-6639
Franz Bauer https://orcid.org/0000-0002-8686-8737
Yi-Kuan Chiang https://orcid.org/0000-0001-6320-261X
Robin Ciardullo https://orcid.org/0000-0002-1328-0211
Arjun Dey https://orcid.org/0000-0002-4928-4003
Caryl Gronwall https://orcid.org/0000-0001-6842-2371
Lucia Guaita https://orcid.org/0000-0002-4902-0075
Yun Huang https://orcid.org/0000-0002-2073-5325
Ho Seong Hwang https://orcid.org/0000-0003-3428-7612
Sang Hyeok Im https://orcid.org/0009-0003-9748-4194
Woong-Seob Jeong https://orcid.org/0000-0002-2770-808X
Shreya Karthikeyan https://orcid.org/0009-0002-6186-0293
Hwihyun Kim https://orcid.org/0000-0003-4770-688X
Seongjae Kim https://orcid.org/0009-0002-3931-6697
Ankit Kumar https://orcid.org/0000-0001-6270-3527
Gautam R. Nagaraj https://orcid.org/0000-0002-0905-342X
Julie Nantais https://orcid.org/0000-0002-7356-0629
Nelson Padilla https://orcid.org/0000-0001-9850-9419
Jaehong Park https://orcid.org/0000-0003-3095-6137
Alexandra Pope https://orcid.org/0000-0001-8592-2706
Roxana Popescu https://orcid.org/0000-0001-8245-7669
David Schlegel https://orcid.org/0000-0002-5042-5088
Eunsuk Seo https://orcid.org/0009-0007-1810-5117
Hyunmi Song https://orcid.org/0000-0002-4362-4070
Paulina Troncoso https://orcid.org/0000-0001-6162-3023
A. Katherina Vivas https://orcid.org/0000-0003-4341-6172
Ann Zabludoff https://orcid.org/0000-0001-6047-8469
Alfredo Zenteno https://orcid.org/0000-0001-6455-9135

References

Adelberger, K. L., Steidel, C. C., Pettini, M., et al. 2005, ApJ, 619, 697
Aihara, H., AlSayyad, Y., Ando, M., et al. 2022, PASJ, 74, 247
Aihara, H., Arimoto, N., Armstrong, R., et al. 2018, PASJ, 70, S4
Annunziatella, M., Sajina, A., Stefanon, M., et al. 2023, AJ, 166, 25
Appleby, S., Park, C., Hong, S. E., & Kim, J. 2017, ApJ, 836, 45
Appleby, S., Park, C., Hong, S. E., & Kim, J. 2018, ApJ, 853, 17
Appleby, S., Park, C., Hong, S. E., et al. 2021, ApJ, 907, 75
Arrigoni Battaia, F., Hennawi, J. F., Prochaska, J. X., et al. 2019, MNRAS, 482, 3162
Baldry, I. K., Balogh, M. L., Bower, R. G., et al. 2006, MNRAS, 373, 469
Bernstein, G. M., Abbott, T. M. C., Desai, S., et al. 2017, PASP, 129, 114502
Bertin, E. 2006, in ASP Conf. Ser. 351, Astronomical Data Analysis Software and Systems XV, ed. C. Gabriel et al. (San Francisco, CA: ASP), 112
Blakeslee, J. P., Franx, M., Postman, M., et al. 2003, ApJL, 596, L143
Bond, J. R., Kofman, L., & Pogosyan, D. 1996, Natur, 380, 603
Borisova, E., Cantalupo, S., Lilly, S. J., et al. 2016, ApJ, 831, 39
Bădescu, T., Yang, Y., Bertoldi, F., et al. 2017, ApJ, 845, 172
Burleigh, K. J., Landriau, M., Dey, A., et al. 2020, AJ, 160, 61
Cantalupo, S., Arrigoni-Battaia, F., Prochaska, J. X., Hennawi, J. F., & Madau, P. 2014, Natur, 506, 63
Casey, C. M. 2016, ApJ, 824, 36
Cen, R., & Zheng, Z. 2013, ApJ, 775, 112
Chang, S.-J., Yang, Y., Seon, K.-I., Zabludoff, A., & Lee, H.-W. 2023, ApJ, 945, 100
Chiang, Y.-K., Overzier, R., & Gebhardt, K. 2013, ApJ, 779, 127
Chiang, Y.-K., Overzier, R., & Gebhardt, K. 2014, ApJL, 782, L3
Ciardullo, R., Gronwall, C., Wolf, C., et al. 2012, ApJ, 744, 110
Cucciati, O., Lemaux, B. C., Zamorani, G., et al. 2018, A&A, 619, A49
Daddi, E., Rich, R. M., Valentino, F., et al. 2022, ApJL, 926, L21
Daddi, E., Valentino, F., Rich, R. M., et al. 2021, A&A, 649, A78
Dey, A., Bian, C., Soifer, B. T., et al. 2005, ApJ, 629, 654
Dey, A., Lee, K.-S., Reddy, N., et al. 2016, ApJ, 823, 11
Dong, F., Park, C., Hong, S. E., et al. 2023, ApJ, 953, 98
Drechsler, M., Strottner, X., Sainty, Y., et al. 2023, RNAAS, 7, 1
Eisenhardt, P. R. M., Brodwin, M., Gonzalez, A. H., et al. 2008, ApJ, 684, 905

Ellison, S. L., Patton, D. R., Simard, L., & McConnachie, A. W. 2008, AJ, 135, 1877
Erb, D. K., Bogosavljević, M., & Steidel, C. C. 2011, ApJL, 740, L31
Euclid Collaboration, Moneti, A., McCracken, H. J., et al. 2022, A&A, 658, A126
Fardal, M. A., Katz, N., Gardner, J. P., et al. 2001, ApJ, 562, 605
Flaugher, B., Diehl, H. T., Honscheid, K., et al. 2015, AJ, 150, 150
Francis, P. J., Woodgate, B. E., Warren, S. J., et al. 1996, ApJ, 457, 490
Gaia Collaboration, Brown, A. G. A., Vallenari, A., et al. 2021, A&A, 649, A1
Gawiser, E., Francke, H., Lai, K., et al. 2007, ApJ, 671, 278
Gawiser, E., van Dokkum, P. G., Gronwall, C., et al. 2006, ApJL, 642, L13
Giavalisco, M., & Dickinson, M. 2001, ApJ, 550, 177
Gronwall, C., Ciardullo, R., Hickey, T., et al. 2007, ApJ, 667, 79
Guaita, L., Acquaviva, V., Padilla, N., et al. 2011, ApJ, 733, 114
Guaita, L., Gawiser, E., Padilla, N., et al. 2010, ApJ, 714, 255
Haiman, Z., Spaans, M., & Quataert, E. 2000, ApJL, 537, L5
Hartley, W. G., Choi, A., Amon, A., et al. 2022, MNRAS, 509, 3547
Hu, E. M., & McMahon, R. G. 1996, Natur, 382, 231
Huang, Y., Lee, K.-S., Cucciati, O., et al. 2022, ApJ, 941, 134
Hwang, H. S., Elbaz, D., Dickinson, M., et al. 2011, A&A, 535, A60
Inoue, A. K., Yamanaka, S., Ouchi, M., et al. 2020, PASJ, 72, 101
Kikuta, S., Ouchi, M., Shibuya, T., et al. 2023, ApJS, 268, 24
Kollmeier, J. A., Zheng, Z., Davé, R., et al. 2010, ApJ, 708, 1048
Kovač, K., Somerville, R. S., Rhoads, J. E., Malhotra, S., & Wang, J. 2007, ApJ, 668, 15
Kusakabe, H., Shimasaku, K., Ouchi, M., et al. 2018, PASJ, 70, 4
Lacy, M., Surace, J. A., Farrah, D., et al. 2021, MNRAS, 501, 892
Laursen, P., & Sommer-Larsen, J. 2007, ApJL, 657, L69
Lee, J., Park, C., Kim, J., et al. 2024, ApJ, 960, 132
Lee, J., Shin, J., Snaith, O. N., et al. 2021, ApJ, 908, 11
Lee, K.-S., Dey, A., Hong, S., et al. 2014, ApJ, 796, 126
Lee, K.-S., Giavalisco, M., Gnedin, O. Y., et al. 2006, ApJ, 642, 63
Lemaux, B. C., Cucciati, O., Le Fèvre, O., et al. 2022, A&A, 662, A33
Lonsdale, C. J., Smith, H. E., Rowan-Robinson, M., et al. 2003, PASP, 115, 897
Madau, P., & Dickinson, M. 2014, ARA&A, 52, 415
Malavasi, N., Lee, K.-S., Dey, A., et al. 2021, ApJ, 921, 103
Mancone, C. L., Gonzalez, A. H., Brodwin, M., et al. 2010, ApJ, 720, 284
Mason, C. A., Treu, T., Dijkstra, M., et al. 2018, ApJ, 856, 2
Matsuda, Y., Yamada, T., Hayashino, T., et al. 2004, AJ, 128, 569
Matsuda, Y., Yamada, T., Hayashino, T., et al. 2011, MNRAS, 410, L13
Mauduit, J. C., Lacy, M., Farrah, D., et al. 2012, PASP, 124, 714
Mei, S., Holden, B. P., Blakeslee, J. P., et al. 2006, ApJ, 644, 759
Merlin, E., Castellano, M., Santini, P., et al. 2021, A&A, 649, A22
Momose, R., Shimasaku, K., Kashikawa, N., et al. 2021, ApJ, 909, 117
Muldrew, S. I., Hatch, N. A., & Cooke, E. A. 2015, MNRAS, 452, 2528
Nayyeri, H., Hemmati, S., Mobasher, B., et al. 2017, ApJS, 228, 7
Noeske, K. G., Weiner, B. J., Faber, S. M., et al. 2007, ApJL, 660, L43
Norberg, P., Baugh, C. M., Hawkins, E., et al. 2002, MNRAS, 332, 827
Oke, J. B., & Gunn, J. E. 1983, ApJ, 266, 713
Ono, Y., Itoh, R., Shibuya, T., et al. 2021, ApJ, 911, 78
Ouchi, M., Harikane, Y., Shibuya, T., et al. 2018, PASJ, 70, S13
Ouchi, M., Ono, Y., & Shibuya, T. 2020, ARA&A, 58, 617
Ouchi, M., Shimasaku, K., Akiyama, M., et al. 2008, ApJS, 176, 301
Ouchi, M., Shimasaku, K., Furusawa, H., et al. 2003, ApJ, 582, 60
Ouchi, M., Shimasaku, K., Furusawa, H., et al. 2010, ApJ, 723, 869
Overzier, R. A. 2016, A&ARv, 24, 14
Overzier, R. A., Nesvadba, N. P. H., Dijkstra, M., et al. 2013, ApJ, 771, 89
Papovich, C., Shipley, H. V., Mehrtens, N., et al. 2016, ApJS, 224, 28
Park, C., & Kim, Y.-R. 2010, ApJL, 715, L185
Park, C., Lee, J., Kim, J., et al. 2022, ApJ, 937, 15
Park, H., Park, C., Sabiu, C. G., et al. 2019, ApJ, 881, 146
Partridge, R. B., & Peebles, P. J. E. 1967, ApJ, 147, 868
Peng, Y.-j., Lilly, S. J., Kovač, K., et al. 2010, ApJ, 721, 193
Planck Collaboration, Aghanim, N., Altieri, B., et al. 2015, A&A, 582, A30
Prescott, M. K. M., Kashikawa, N., Dey, A., & Matsuda, Y. 2008, ApJL, 678, L77
Ramakrishnan, V., Moon, B., Im, S. H., et al. 2023, ApJ, 951, 119
Reiprich, T. H., & Böhringer, H. 2002, ApJ, 567, 716
Saito, T., Shimasaku, K., Okamura, S., et al. 2006, ApJ, 648, 54
Sawicki, M., Arnouts, S., Huang, J., et al. 2019, MNRAS, 489, 5202
Schlafly, E. F., Finkbeiner, D. P., Jurić, M., et al. 2012, ApJ, 756, 158
Sheth, R. K., Mo, H. J., & Tormen, G. 2001, MNRAS, 323, 1
Shi, K., Lee, K.-S., Dey, A., et al. 2019, ApJ, 871, 83
Sobral, D., Santos, S., Matthee, J., et al. 2018, MNRAS, 476, 4725
Speare, R., Gott, J. R., Kim, J., & Park, C. 2015, ApJ, 799, 176
Springel, V., White, S. D. M., Jenkins, A., et al. 2005, Natur, 435, 629
Stanford, S. A., Eisenhardt, P. R., & Dickinson, M. 1998, ApJ, 492, 461
Steidel, C. C., Adelberger, K. L., Giavalisco, M., Dickinson, M., & Pettini, M. 1999, ApJ, 519, 1
Steidel, C. C., Adelberger, K. L., Shapley, A. E., et al. 2000, ApJ, 532, 170
Stevans, M. L., Finkelstein, S. L., Kawinwanichakij, L., et al. 2021, ApJ, 921, 58
Taniguchi, Y., & Shioya, Y. 2000, ApJL, 532, L13
Thomas, D., Maraston, C., Bender, R., & Mendes de Oliveira, C. 2005, ApJ, 621, 673
Topping, M. W., Shapley, A. E., Steidel, C. C., Naoz, S., & Primack, J. R. 2018, ApJ, 852, 134
Toshikawa, J., Uchiyama, H., Kashikawa, N., et al. 2018, PASJ, 70, S12
Umehata, H., Fumagalli, M., Smail, I., et al. 2019, Sci, 366, 97
Valdes, F. 2021, The DECam Community Pipeline Instrumental Signature Removal, https://legacy.noirlab.edu/noao/staff/fvaldes/Pipelines/Docs/PL206/
Valdes, F., Gruendl, R. & DES Project 2014, in ASP Conf. Ser. 485, Astronomical Data Analysis Software and Systems XXIII, ed. N. Manset & P. Forshay (San Francisco, CA: ASP), 379
van der Burg, R. F. J., Rudnick, G., Balogh, M. L., et al. 2020, A&A, 638, A112
Vargas, C. J., Bish, H., Acquaviva, V., et al. 2014, ApJ, 783, 26
Weaver, J. R., Kauffmann, O. B., Ilbert, O., et al. 2022, ApJS, 258, 11
Weinberger, L. H., Haehnelt, M. G., & Kulkarni, G. 2019, MNRAS, 485, 1350
Weinberger, R., Springel, V., Hernquist, L., et al. 2017, MNRAS, 465, 3291
Weiss, L. H., Bowman, W. P., Ciardullo, R., et al. 2021, ApJ, 912, 100
Wold, I. G. B., Kawinwanichakij, L., Stevans, M. L., et al. 2019, ApJS, 240, 5
Xue, R., Lee, K.-S., Dey, A., et al. 2017, ApJ, 837, 172
Yang, X., Mo, H. J., & van den Bosch, F. C. 2009, ApJ, 695, 900
Yang, Y., Walter, F., Decarli, R., et al. 2014, ApJ, 784, 171
Yang, Y., Zabludoff, A., Eisenstein, D., & Davé, R. 2010, ApJ, 719, 1654
York, D. G., Adelman, J., Anderson, J. E., Jr., et al. 2000, AJ, 120, 1579
Zabl, J., Freudling, W., Møller, P., et al. 2016, A&A, 590, A66